Normalizing flow neural networks by JKO scheme

Chen Xu
School of Industrial and Systems Engineering
Georgia Tech

Xiuyuan Cheng
Department of Mathematics
Duke University

Yao Xie
School of Industrial and Systems Engineering
Georgia Tech

Abstract

Normalizing flow is a class of deep generative models for efficient sampling and likelihood estimation, which achieves attractive performance, particularly in high dimensions. The flow is often implemented using a sequence of invertible residual blocks. Existing works adopt special network architectures and regularization of flow trajectories. In this paper, we develop a neural ODE flow network called JKO-iFlow, inspired by the Jordan-Kinderleherer-Otto (JKO) scheme, which unfolds the discrete-time dynamic of the Wasserstein gradient flow. The proposed method stacks residual blocks one after another, allowing efficient block-wise training of the residual blocks, avoiding sampling SDE trajectories and score matching or variational learning, thus reducing the memory load and difficulty in end-to-end training. We also develop adaptive time reparameterization of the flow network with a progressive refinement of the induced trajectory in probability space to improve the model accuracy further. Experiments with synthetic and real data show that the proposed JKO-iFlow network achieves competitive performance compared with existing flow and diffusion models at a significantly reduced computational and memory cost.

1 Introduction

Generative models have wide applications in statistics and machine learning to infer data-generating distributions and to sample from the model distributions learned from the data. In addition to widely used deep generative models such as variational auto-encoders (VAE) Kingma and Welling [2014, 2019] and generative adversarial networks (GAN) Goodfellow et al. [2014], Gulrajani et al. [2017], normalizing flow models Kobyzev et al. [2020] have been popular and with a great potential. The flow model learns the data distribution via an invertible mapping F between the data density p_X in $\mathbb{R}^d$ and the target standard multivariate Gaussian density p_Z, $Z \sim \mathcal{N}(0, I_d)$. While flow models, once trained, can be utilized for efficient data sampling and explicit likelihood evaluation, training of such models is often difficult in practice. To alleviate such difficulties, many prior works [Dinh et al., 2015, 2017, Kingma and Dhariwal, 2018, Behrmann et al., 2019, Ruthotto et al., 2020, Onken et al., 2021], among others, have explored designs of training objectives, network architectures, and computational techniques.

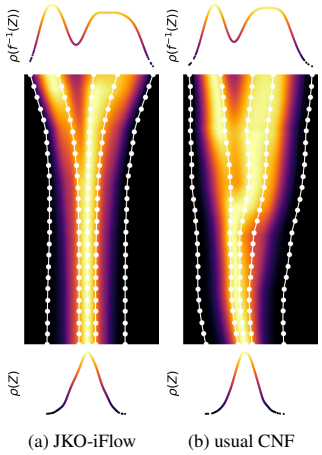

(a) JKO-iFlow (b) usual CNF

Figure 1: Comparison of JKO-iFlow (proposed) and standard CNF models. In contrast to most existing CNF models, JKO-iFlow learns the unique deterministic transport equation corresponding to the diffusion process by directly performing block-wise training of a neural ODE model.

Among various flow models, continuous normalizing flow (CNF) transports the data density to a target distribution through continuous dynamics, primarily neural ODE [Chen et al., 2018] models.

Accepted to the Optimal Transport and Machine Learning Workshop at NeurIPS 2023.

However, a known computational challenge of CNF models is model regularization, primarily due to the non-uniqueness of the flow transport. Without additional regularization, the trained CNF model such as FFJORD Grathwohl et al. [2019] may follow a less regular trajectory in the probability space, see Figure 1(b), which may worsen the generative performance. While regularization of flow models has been developed using different techniques, including using spectral normalization Behrmann et al. [2019] and optimal transport Onken et al. [2021], Xu et al. [2022], only using regularization may not resolve the non-uniqueness of the flow. Besides regularization, several practical difficulties remain when training CNF models, particularly the high computational cost: In many settings, CNF models consist of stacked blocks and each can be complex. End-to-end training of such deep models often places a high demand on computational resources and memory consumption.

In this work, we propose JKO-iFlow, an invertible normalizing flow network that unfolds the Wasserstein gradient flow via a neural ODE model inspired by the JKO-scheme Jordan et al. [1998]. The JKO scheme, see (5), can be viewed as a proximal step to minimize the KullbackLeibler (KL) divergence between the current density and the equilibrium density. It recovers the solution of the Fokker-Planck equation (FPE) in the limit of small step size. The proposed JKO-iFlow model thus can be viewed as trained to learn the *unique* transport map following the FPE which flows from the data distribution toward the normal equilibrium and gives a smooth trajectory of density evolution, see Figure 1(a). In summary, the contributions of the work include

• We propose an invertible neural ODE model where each residual block corresponds to a JKO step, and the training objective can be computed from pushed data samples through the previous blocks. The residual block has a general form, and the invertibility is ensured due to the regularity and continuity of the approximate solution of the FPE.

• We develop a block-wise procedure to train the JKO-iFlow model which can determine the number of blocks adaptively. We also propose to adaptively reparameterize the computed trajectory in the probability space with refinement, which improves the model accuracy and the overall computational efficiency.

• We show that JKO-iFlow greatly reduces memory and computational cost when achieving competitive or better generative performance and likelihood estimation compared to existing flow and diffusion models on simulated and real data.

1.1 Related works

The normalizing flow framework [Kobyzev et al., 2020] has been extensively developed, including continuous flow [Grathwohl et al., 2019], Monge-Ampere flow [Zhang et al., 2018], discrete flow [Chen et al., 2019], and extension to non-Euclidean data [Liu et al., 2019, Mathieu and Nickel, 2020, Xu et al., 2022]. Efforts have been made to develop novel invertible mapping structures [Dinh et al., 2017, Papamakarios et al., 2017] and regularize the flow trajectories by transport cost [Finlay et al., 2020, Onken et al., 2021, Ruthotto et al., 2020, Xu et al., 2022, Huang et al., 2023]. Despite such efforts, the model and computational challenges of normalizing flow models include regularization and the large model size when using a large number of residual blocks, which cannot be determined a priori, and the associated memory and computational load.

In parallel to neural ODE CNF models, neural SDE models become an emerging tool for generative tasks. Diffusion process and Langevin dynamics in deep generative models have been studied in score-based generative models [Song and Ermon, 2019, Ho et al., 2020, Block et al., 2020, Song et al., 2021] under different settings. Specifically, these models estimate the score function of data distribution via neural network parametrization, which may encounter challenges in learning and sampling of high dimensional data and call for special techniques [Song and Ermon, 2019]. The recent work of Song et al. [2021] developed reverse-time SDE sampling for score-based generative models and adopted the connection to neural ODE to compute the likelihood; using the same idea of backward SDE, Zhang and Chen [2021] proposed joint training of forward and backward neural SDEs. The current work focuses on a neural ODE model where the deterministic vector field $\mathbf{f}(x, t)$ is to be learned from data following a JKO scheme of the FPE. Rather than neural SDE, our approach involves no sampling of SDE trajectories nor learning of the score function, and it learns an invertible residual network directly. We experimentally obtain competitive or improved performance against the diffusion model on simulated 2D data and high-dimensional tabular data.

JKO-inspired deep models have been studied in several recent works. [Bunne et al., 2022] reformulated the JKO step for minimizing an energy function over convex functions. JKO scheme has also been used to discretize Wasserstein gradient flow to learn a deep generative model in [Alvarez-Melis et al., 2022, Mokrov et al., 2021], which adopted input convex neural networks (ICNN) [Amos et al., 2017]. ICNN, as a special type of network architecture, may have limited expressiveness [Rout et al., 2022, Korotin et al., 2021]. In addition to using the gradient of ICNN, [Fan et al., 2022] proposed to parametrize the transport in a JKO step by a residual network but identified difficulty in calculating the push-forward distribution. Our method trains an invertible neural-ODE flow network that flows from data density to the normal one and backward, which enables the computation of model likelihood as in other neural-ODE approaches. The objective in each JKO step to minimize KL divergence can also be computed directly, see Section 4.

Compared to score-based neural SDE methods, our approach is closer to the more recent flow-based models that are related to diffusion models [Lipman et al., 2023, Albergo and Vanden-Eijnden, 2023, Boffi and Vanden-Eijnden, 2023]. These works proposed to learn the transport equation (a deterministic ODE) corresponding to the SDE process. Specifically, [Lipman et al., 2023, Albergo and Vanden-Eijnden, 2023] matched the velocity field from interpolated distributions between initial and terminal ones; [Boffi and Vanden-Eijnden, 2023] proposed to learn the score $\nabla \log \rho_t(x)$ (where ρ_t solves the FPE and is unknown *a priori*) to solve high-dimensional FPE. The idea of approximating the solution of FPE by a deterministic transport equation dates back to the 90s Degond and Mustieles [1990], Degond and Mas-Gallic [1989]. While our approach learns an equivalent velocity field at the infinitesimal time step, see section 3.2, the formulation in JKO-iFlow is at a finite time-step motivated by the JKO scheme. An independent concurrent work also [Vidal et al., 2023] proposed a similar block-wise training algorithm using JKO scheme under the framework of [Onken et al., 2021] and demonstrated benefits in avoiding tuning the penalty hyperparameter in front of the KL-divergence objective. Our model is applied to generative tasks of high-dimensional data including image data, and we also develop additional techniques for computing the flow probability trajectory.

2 Preliminaries

Normalizing flow. A normalizing flow can be mathematically expressed via a density evolution equation of $\rho(x,t)$ such that $\rho(x,0) = p_X$ and as t increases $\rho(x,t)$ approaches $p_Z \sim \mathcal{N}(0, I_d)$ [Tabak and Vanden-Eijnden, 2010]. Given an initial distribution $\rho(x,0)$, such a flow typically is not unique. We consider when the flow is induced by an ODE of $x(t)$ in $\mathbb{R}^d$

$$\dot{x}(t) = \mathbf{f}(x(t), t), \tag{1}$$

where $x(0) \sim p_X$. The marginal density of $x(t)$ is denoted as $p(x,t)$, and it evolves according to the continuity equation (Liouville equation) of (1) written as

$$\partial_t p + \nabla \cdot (p\mathbf{f}) = 0, \quad p(x,0) = p_X(x). \tag{2}$$

OrnsteinUhlenbeck (OU) process. Consider a Langevin dynamic denoted by the SDE $dX_t = -\nabla V(X_t)dt + \sqrt{2}dW_t$, where V is the potential of the equilibrium density p_Z. We focus on the case of normal equilibrium, that is, $V(x) = |x|^2/2$ and then $p_Z \propto e^{-V}$. In this case, the process is known as the (multivariate) OU process. Suppose $X_0 \sim p_X$, and let the density of X_t be $\rho(x,t)$ also denoted as $\rho_t(\cdot)$. The Fokker-Planck equation (FPE) describes the evolution of ρ_t towards the equilibrium p_Z as follows, where $V(x) := |x|^2/2$,

$$\partial_t \rho = \nabla \cdot (\rho \nabla V + \nabla \rho), \quad \rho(x,0) = p_X(x). \tag{3}$$

Under generic conditions, ρ_t converges to p_Z exponentially fast. For Wasserstein-2 distance and the standard normal p_Z, classical argument gives that (take $C = 1$ in Eqn (6) of Bolley et al. [2012])

$$W_2(\rho_t, p_Z) \leq e^{-t} W_2(\rho_0, p_Z), \quad t > 0. \tag{4}$$

JKO scheme. The seminal work Jordan et al. [1998] established a time discretization scheme of the solution to (3) by the gradient flow to minimize $\mathrm{KL}(\rho || p_Z)$ under the Wasserstein-2 metric in probability space. Denote by $\mathcal{P}$ the space of all probability densities on $\mathbb{R}^d$ with a finite second moment. The JKO scheme computes a sequence of distributions p_k, $k = 0, 1, \cdots$, starting from $p_0 = \rho_0 \in \mathcal{P}$. With step size $h > 0$, the scheme at the k-th step is written as

$$p_{k+1} = \arg\min_{\rho \in \mathcal{P}} F[\rho] + \frac{1}{2h} W_2^2(p_k, \rho), \tag{5}$$

where $F[\rho] := \mathrm{KL}(\rho||p_Z)$. It was proved in Jordan et al. [1998] that as $h \to 0$, the solution p_k converges to the solution $\rho(\cdot, kh)$ of (3) for all k, and the convergence $\rho_{(h)}(\cdot, t) \to \rho(\cdot, t)$ is strongly in $L^1(\mathbb{R}^d, (0, T))$ for finite T where $\rho_{(h)}$ is piece-wise constant interpolated from p_k.

3 JKO scheme by neural ODE

Given i.i.d. observed data samples $X_i \in \mathbb{R}^d$, $i = 1, \ldots, N$, drawn from some unknown density p_X, the goal is to train an invertible neural network to transport the density p_X to an *a priori* specified density p_Z in $\mathbb{R}^d$, where each data sample X_i is mapped to a code Z_i. A prototypical choice of p_Z is the standard multivariate Gaussian $\mathcal{N}(0, I_d)$. In this work, we leave the potential of p_Z abstract and denote by V, that is, $p_Z \propto e^{-V}$ and $V(x) = |x|^2/2$ for normal p_Z. By a slight abuse of notation, we denote by p_X and p_Z both the distributions and the density functions of data X and code Z respectively.

3.1 The objective of JKO step

We are to specify $\mathbf{f}(x, t)$ in the ODE (1), to be parametrized and learned by a neural ODE, such that the induced density evolution of $p(x, t)$ converges to p_Z as t increases. We start by dividing the time horizon $[0, T]$ into finite subintervals with step size h, let $t_k = kh$ and $I_{k+1} := [t_k, t_{k+1})$. Define $p_k(x) := p(x, kh)$, namely the density of $x(t)$ at $t = kh$. The solution of (1) determined by the vector-field $\mathbf{f}(x, t)$ on $t \in I_{k+1}$ (assuming the ODE is well-posed [Sideris, 2013]) gives a one-to-one mapping T_{k+1} on $\mathbb{R}^d$, s.t. $T_{k+1}(x(t_k)) = x(t_{k+1})$ and T_{k+1} transports p_k into p_{k+1}, i.e., $(T_k)_{\#}p_{k-1} = p_k$, where we denote by $T_{\#}p$ the push-forward of distribution p by T, such that $(T_{\#}p)(A) = p(T^{-1}(A))$ for a measurable set A. In other words, the mapping T_{k+1} is the solution map of the ODE from time t_k to t_{k+1}.

Suppose we can find $\mathbf{f}(\cdot, t)$ on I_{k+1} such that the corresponding T_{k+1} solves the JKO scheme (5), then with small h, p_k approximates the solution to the Fokker-Planck equation 3, which then flows towards p_Z. By the Monge formulation of the Wasserstein-2 distance between p and q as $W_2^2(p, q) = \min_{T:T_{\#}p=q} \mathbb{E}_{x\sim p}\|x - T(x)\|^2$, solving for the transported density p_k by (5) is equivalent to solving for the transport T_{k+1} by

$$T_{k+1} = \arg\min_{T:\mathbb{R}^d \to \mathbb{R}^d} F[T] + \frac{1}{2h}\mathbb{E}_{x\sim p_k}\|x - T(x)\|^2, \tag{6}$$

where $F[T] = \mathrm{KL}(T_{\#}p_k||p_Z)$. The equivalence between (5) and (6) is proved in Lemma A.1.

Furthermore, the following proposition gives that, once p_k is determined by $\mathbf{f}(x, t)$ for $t \leq t_k$, the value of $F[T]$ can be computed from $\mathbf{f}(x, t)$ on $t \in I_{k+1}$ only. The counterpart for convex function-based parametrization of T_k was given in Theorem 1 of [Mokrov et al., 2021], where the computation using the change-of-variable differs as we adopt an invertible neural ODE approach here. The proof is left to Appendix A.

Proposition 3.1. *Given p_k, up to a constant c independent from $\mathbf{f}(x, t)$ on $t \in I_{k+1}$,*

$$\mathrm{KL}(T_{\#}p_k||p_Z) = \mathbb{E}_{x(t_k)\sim p_k}\left(V(x(t_{k+1})) - \int_{t_k}^{t_{k+1}} \nabla \cdot \mathbf{f}(x(s), s)ds\right) + c. \tag{7}$$

By Proposition 3.1, the minimization (6) is equivalent to

$$\min_{\{\mathbf{f}(x,t)\}_{t\in I_{k+1}}} \mathbb{E}_{x(t_k)\sim p_k}\big(V(x(t_{k+1})) - \int_{t_k}^{t_{k+1}} \nabla \cdot \mathbf{f}(x(s), s)ds + \frac{1}{2h}\|x(t_{k+1}) - x(t_k)\|^2\big), \tag{8}$$

where $x(t_{k+1}) = x(t_k) + \int_{t_k}^{t_{k+1}} \mathbf{f}(x(s), s)ds$. Taking a neural ODE approach, we parametrize $\{\mathbf{f}(x, t)\}_{t\in I_{k+1}}$ as a residual block with parameter θ_{k+1}, and then (8) is reduced to minimizing over θ_{k+1}. This leads to block-wise learning algorithm to be introduced in Section 4, where we furtherly allow the step-size h to vary for different k as well.

3.2 Infinitesimal optimal $\mathbf{f}(x, t)$

In each JKO step of (8), let $p = p_k$ denote the current density, $q = p_Z$ be the target equilibrium density. In this subsection, we show that the optimal $\mathbf{f}$ in (8) with small h reveals the difference

between score functions between target and current densities. Thus minimizing the objective (8) searches for a neural network parametrization of the score function $\nabla \log \rho_t$ implicitly, in contrast to diffusion-based models which learn the score function explicitly [Ho et al., 2020, Song et al., 2021], e.g. via denoising score matching. At infinitesimal h, this is equivalent to solving FPK by learning a deterministic transport equation as in [Boffi and Vanden-Eijnden, 2023, Shen et al., 2022].

Consider general equilibrium distribution q with a differentiable potential V. To analyze the optimal pushforward mapping in the small h limit, we shift the time interval $[kh, (k+1)h]$ to be $[0, h]$ to simplify notation. Then (8) is reduced to

$$\min_{\{\mathbf{f}(x,t)\}_{t\in[0,h)}} \mathbb{E}_{x(0)\sim p}\left(V(x(h)) - \int_0^h \nabla\cdot\mathbf{f}(x(s),s)ds + \frac{1}{2h}\|x(h)-x(0)\|^2\right), \tag{9}$$

where $x(h) = x(0) + \int_0^h \mathbf{f}(x(s),s)ds$. In the limit of $h \to 0+$, formally, $x(h) - x(0) = h\mathbf{f}(x(0),0) + O(h^2)$, and suppose V of q is C^2, $V(x(h)) = V(x(0)) + h\nabla V(x(0))\cdot\mathbf{f}(x(0),0) + O(h^2)$. For any differentiable density ρ, the (Stein) score function is defined as $\mathbf{s}_\rho = \nabla\log\rho$, and we have $\nabla V = -\mathbf{s}_q$. Taking the formal expansion of orders of h, the objective in (9) is written as

$$\mathbb{E}_{x\sim p}\left(V(x) + h\left(-\mathbf{s}_q(x)\cdot\mathbf{f}(x,0) - \nabla\cdot\mathbf{f}(x,0) + \frac{1}{2}\|\mathbf{f}(x,0)\|^2\right) + O(h^2)\right). \tag{10}$$

Note that $\mathbb{E}_{x\sim p}V(x)$ is independent of $\mathbf{f}(x,t)$, and the $O(h)$ order term in (10) is over $\mathbf{f}(x,0)$ only, thus the minimization of the leading term is equivalent to

$$\min_{\mathbf{f}(\cdot)=\mathbf{f}(\cdot,0)} \mathbb{E}_{x\sim p}\left(-T_q\mathbf{f} + \frac{1}{2}\|\mathbf{f}\|^2\right), \quad T_q\mathbf{f} := \mathbf{s}_q\cdot\mathbf{f} + \nabla\cdot\mathbf{f}, \tag{11}$$

where T_q is known as the Stein operator [Stein, 1972]. The $T_q\mathbf{f}$ in (11) echoes that the derivative of KL divergence with respect to transport map gives Stein operator [Liu and Wang, 2016]. The Wasserstein-2 regularization gives an L^2 regularization in (11). Let $L^2(p)$ be the L^2 space on $(\mathbb{R}^d, p(x)dx)$, and for vector field $\mathbf{v}$ on $\mathbb{R}^d$, $\mathbf{v}\in L^2(p)$ if $\int|\mathbf{v}(x)|^2p(x)dx < \infty$. One can verify that, when both $\mathbf{s}_p$ and $\mathbf{s}_q$ are in $L^2(p)$, the minimizer of (11) is $\mathbf{f}^*(\cdot,0) = \mathbf{s}_q - \mathbf{s}_p$.

4 Training of JKO-iFlow net

The proposed JKO-iFlow model allows progressive learning of the residual blocks in the neural-ODE model in a block-wise manner (Section 4.1). We also introduce two techniques to improve the training of the trajectories in probability space (Section 4.2), illustrated in a vector space in Appendix B.3.

4.1 Block-wise training

Note that the training of $(k+1)$-th block in (8) can be conducted once the previous k blocks are trained. Specifically, with finite training data $\{X_i = x_i(0)\}_{i=1}^n$, the expectation $\mathbb{E}_{x(t)\sim p_k}$ in (8) is replaced by the sample average over $\{x_i(kh)\}_{i=1}^n$ which can be computed from the previous k blocks. Note that for each given $x(t) = x(t_k)$, both $x(t_{k+1})$ and the integral of $\nabla\cdot\mathbf{f}$ in (8) can be computed by a numerical neural ODE integrator. Following previous works, we use the Hutchinson trace estimator [Hutchinson, 1989, Grathwohl et al., 2019] to compute the quantity $\nabla\cdot\mathbf{f}$ in high dimensions, and we also propose a finite-difference approach to reduce the computational cost (details in Appendix B.2). Applying the numerical integrator in computing (8), we denote the resulting k-th residual block abstractly as f_{θ_k} with trainable parameters θ_k.

Algorithm 1 Block-wise JKO-iFlow training

Require: Time stamps $\{t_k\}$, training data, termination criterion Ter and tolerance level ϵ, maximal number of blocks $L_{\max}$.

Initialize $k = 1$.
while $\mathrm{Ter(k)} > \epsilon$ and $k \le L_{\max}$ **do**
  Optimize f_{θ_k} upon minimizing (8) with mini-batch sample approximation, given $\{f_{\theta_i}\}_{i=1}^{k-1}$. Set $k \leftarrow k+1$.
end while
$L \leftarrow k$. Optional: Optimize $f_{\theta_{L+1}}$ without W_2 regularization.

This leads to a block-wise training of the normalizing flow network, as summarized in Algorithm 1. The sequence of time stamps t_k is given by specifying the time steps $h_k := t_{k+1} - t_k$, which we allow

to differ across k. The choice of the sequence h_k is initialized by a geometric sequence starting from h_0 with maximum stepsize $h_{\max}$, see Appendix B.1. In the special case where the multiplying factor is one, the sequence of h_k gives a constant step size. The adaptive choice of h_k with refinement (by adding more blocks) is to be introduced in Section 4.2. Regarding the termination criterion $\mathrm{Ter(k)}$ in line 2 of Algorithm 1, we monitor the ratio $\mathbb{E}_{x\sim p_{k-1}}\|x - T_k(x)\|^2/\mathbb{E}_{x\sim p_{k-1}}\|T_k(x)\|^2$ and terminate when it is below some threshold ϵ, set as 0.01 in all experiments. In practice, when training the k-th block, both the averages of $\|x - T_k(x)\|^2$ and $\|T_k(x)\|^2$ are computed by empirically averaging over the training samples (in the last epoch) at no additional computational cost. Lastly, line 5 of training a "free block" (i.e., block without the W_2 regularization) is to flow the push-forward density p_L closer to the target density p_Z, where the former is obtained through the first L blocks.

The block-wise training significantly reduces the memory and computational load since only one block is trained when optimizing (8) regardless of flow depth. Therefore, one can use larger training batches and potentially more expensive numerical integrators within a certain memory budget for higher accuracy. We also empirically observe that training each block using standard back-propagation (rather than the adjoint method in neural ODE) gives a comparable result at a lower cost. To ensure the the invertibility of the trained JKO-iFlow network, we furtherly break the time interval $[t_{k-1}, t_k)$ into 3 or 5 subintervals to compute the neural ODE integration, e.g., by Runge-Kutta-4. We empirically verify the smallness of inversion errors on test samples.

4.2 Computation of trajectories in probability space

We adopt two additional computational techniques to facilitate learning of the trajectories in the probability space, represented by the sequence of densities p_k, $k = 1, \cdots, L$, associated with the L residual blocks of JKO-iFlow. The two techniques are illustrated in Figure A.1. Further details and illustrations of the approach can be found in Appendix B.

• *Trajectory reparameterization*. We empirically observe fast decay of the movements $W_2^2(T_\# p_k, p_k)$ when h_k is set to be constant, that is, initial blocks transport the densities much further than the later ones. This is unwanted in algorithm because the later blocks trained using constant step size barely contribute to the density transport. Hence, we *reparameterize* the values of t_k through an adaptive procedure based on the W_2 distance at each block. The adaptive procedure uses an interactive approach to encourage the W2 movement in each block to be more even across the L blocks, where the retraining of the trajectory can be potentially warm-started by the previous trajectory in iteration.

• *Progressive refinement*. The performance of CNF models is typically improved with larger number of residual blocks, corresponding to smaller step size. However, directly training the model with a small non-adaptive stepsize h may result in long computation time. We introduce a refinement approach to increase the number of blocks progressively, where each time interval $[t_{k-1}, t_k)$ splits into two halves and the number of blocks doubles after the adaptive reparameterization of the trajectory converges at the coarse level. The new trajectory at the refined level is again trained with adaptive reparameterization, where the residual blocks can be warm-started from the coarse-level model to accelerate the convergence.

5 Experiment

In this section, we examine the proposed JKO-iFlow model on simulated and real datasets, including both unconditional and conditional generation tasks.

5.1 Baselines and metrics

We compare with five alternatives, including four flow models and one diffusion model. The first two CNF models are FFJORD [Grathwohl et al., 2019] and OT-Flow [Onken et al., 2021]. The next two discrete-time models are IResNet [Behrmann et al., 2019] and IGNN [Xu et al., 2022]. The diffusion model baseline is the score-based neural SDE [Song et al., 2021], which we call 'ScoreSDE'. Details about the experimental setup can be found in Appendix C.2. The accuracy of trained generative models is evaluated by two quantitative metrics, the negative log-likelihood (NLL) metric, and the kernel *maximum mean discrepancy* (MMD) [Gretton et al., 2012a] metric, including MMD-1, MMD-m, and MMD-c for constant, median distance, and custom bandwidth respectively.

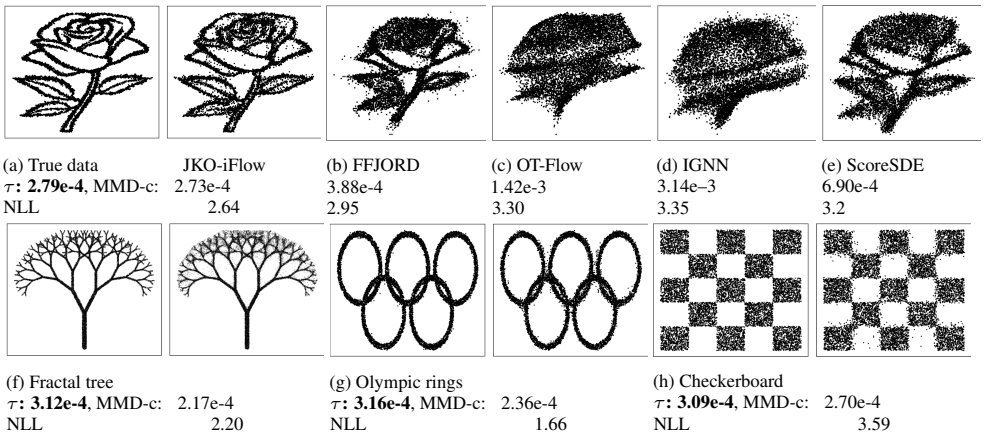

Figure 2: Results on two-dimensional simulated datasets by JKO-iFlow and competitors.

The test threshold τ is computed by bootstrap. See details in Appendix C.1. The numerical inversion error of the trained flow models are at the 1e-5 level or below, see Table A.1.

5.2 Two-dimensional toy data

The results on four toy datasets are shown in Figure 2, where the metrics of NLL and MMD-c are reported. Plots (a)-(e) compare JKO-iFlow with the alternative models on the dataset Rose, where both NLL and MMD-c metrics show the better performance of JKO-iFlow. Visually, the generated samples $\hat{X}$ by JKO-iFlow also more resemble the true data distribution of X than the competitors in (b)-(e). Plots (f)-(h) show the results by JKO-iFlow on the examples of Fractal tree, Olympic rings, and Checkerboard, where JKO-iFlow gives satisfactory generative performance. The results of JKO-iFlow in Figure 2 are obtained after applying the trajectory improvement techniques in Section 4.2. The comparison to without using the techniques is provided in Figures A.3 and A.4, which shows the benefit of the two techniques in learning the model.

5.3 High-dimensional tabular data

Table 1 assesses the performance of JKO-iFlow and baseline methods on four high-dimensional tabular datasets under a fixed-budget setting: we keep the model size of continuous flow models (OT-Flow and FFJORD) and the diffusion model (ScoreSDE) the same, and we increase model sizes for discrete flow models (IGNN and IResNet) which can be computed faster therein and this also improves their performances. Except for MINIBOONE dataset, JKO-iFlow yields smaller or similar quantitative metrics compared to all alternatives. The visual comparisons of generated data distributions are shown in Figure A.6. After additional training to apply the trajectory reparametrization, the performance of JKO-iFlow is furtherly improved, see Table A.4 in comparison with additional baselines of OT-Flow and FFJORD from the original references. The effects of trajectory reparameterization on MINIBOONE dataset are shown in Figure A.5, where the W_2 movements across the blocks become more even as the iteration proceeds, see (a). The generative performance as shown in (b) visually improves after the reparametrization, which is consistent with the lower NLL values in Table A.4

Table 1: Results on tabular datasets. All competitors are trained in a fixed-budget setup using 10 times more mini-batches (their performances using the same number of mini-batches are worse and not comparable to JKO-iFlow). See the complete table in Table A.2. The results using more computation are given in Table A.4.

Data Set	Model	# Param	Test MMD-m	Test MMD-1	NLL
			τ: **1.73e-4**	τ: **2.90e-4**	
POWER $d = 6$	JKO-iFlow	76K	9.86e-5	2.40e-4	-0.12
	OT-Flow	76K	7.58e-4	5.35e-4	0.32
	FFJORD	76K	9.89e-4	1.16e-3	0.63
	IGNN	304K	1.93e-3	1.59e-3	0.95
	IResNet	304K	3.92e-3	2.43e-2	3.37
	ScoreSDE	76K	9.12e-4	6.08e-3	3.41
			τ: **1.85e-4**	τ: **2.73e-4**	
GAS $d = 8$	JKO-iFlow	76K	1.52e-4	5.00e-4	-7.65
	OT-Flow	76K	1.99e-4	5.16e-4	-6.04
	FFJORD	76K	1.87e-3	3.28e-3	-2.65
	IGNN	304K	6.74e-3	1.43e-2	-1.65
	IResNet	304K	3.20e-3	2.73e-2	-1.17
	ScoreSDE	76K	1.05e-3	8.36e-4	-3.69

Data Set	Model	# Param	Test MMD-m	Test MMD-1	NLL
			τ: **2.46e-4**	τ: **3.75e-4**	
MINIBOONE $d = 43$	JKO-iFlow	112K	9.66e-4	3.79e-4	12.55
	OT-Flow	112K	6.58e-4	3.79e-4	11.44
	FFJORD	112K	3.51e-3	4.12e-4	23.77
	IGNN	448K	1.21e-2	4.01e-4	26.45
	IResNet	448K	2.13e-3	4.16e-4	22.36
	ScoreSDE	112K	5.86e-1	4.33e-4	27.38
			τ: **1.38e-4**	τ: **1.01e-4**	
BSDS300 $d = 63$	JKO-iFlow	396K	2.24e-4	1.91e-4	-153.82
	OT-Flow	396K	5.43e-1	6.49e-1	-104.62
	FFJORD	396K	5.60e-1	6.76e-1	-37.80
	IGNN	990K	5.64e-1	6.86e-1	-37.68
	IResNet	990K	5.50e-1	5.50e-1	-33.11
	ScoreSDE	396K	5.61e-1	6.60e-1	-7.55

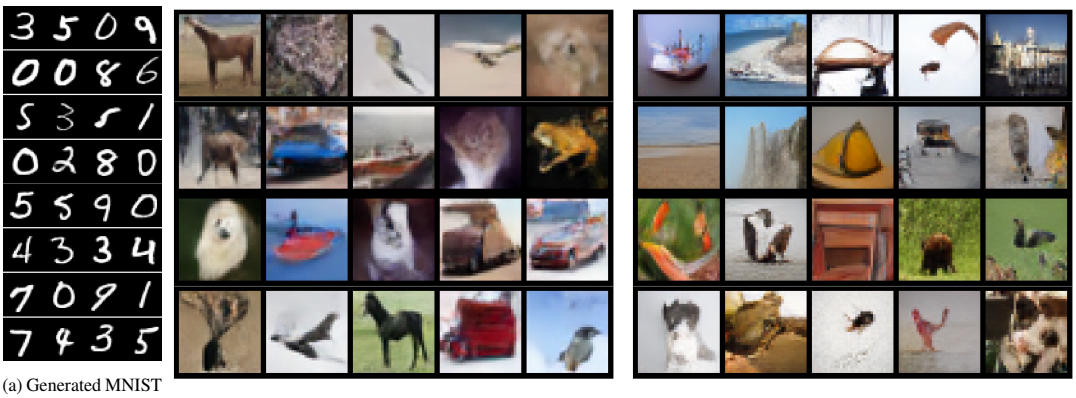

(a) Generated MNIST digits. FID: 7.95.

(b) Generated CIFAR10 images. FID: 29.10.

(c) Generated Imagenet-32 images. FID: 20.10.

Figure 3: Generated samples of MNIST, CIFAR10, and Imagenet-32 by JKO-iFlow model in latent space. We select 2 images per class for CIFAR10 and 1 image per class for Imagenet-32. The FIDs are shown in subcaptions. Uncurated samples are shown in Figure A.7.

(NLL improves from 12.55 to 10.55). These results show that JKO-iFlow performs comparably to the best baseline, and often better under small computational and memory budgets.

5.4 Image generation

We apply the JKO-iFlow model to image generation tasks on the MNIST, CIFAR-10, and Imagenet-32 datasets. In all examples, we train JKO-iFlow in the latent space of a pre-trained variational auto-encoder (VAE) adopted from [Esser et al., 2021]. Training generative models in latent space have been shown to obtain state-of-the-art image generation performance e.g. in StableDiffusion [Rombach et al., 2022]. Here we train a flow model instead of a score-based diffusion model in the latent space, and more details can be found in Appendix C.2. The generated images are shown in Figure 3. The quantitative evaluation is by the Fréchet inception distance (FID) score [Heusel et al., 2017], which is included in the figure captions. Comparatively, we are aware of some performance gap between our model and the state-of-the-art performance of score-based diffusion models like DDPM [Ho et al., 2020] and ScoreSDE [Song et al., 2021], however, the results here are obtained with less computation. Specifically, on a single A100 GPU, our experiments took 24 hours on CIFAR10 and 30 hours on Imagenet-32. Meanwhile, the image generation by JKO-iFlow model here obtains visually more appealing images and achieves lower FIDs compared to most CNF baselines [Grathwohl et al., 2019, Behrmann et al., 2019, Chen et al., 2019, Finlay et al., 2020].

5.5 Conditional generation

The problem aims to generate input samples X given a label Y from the conditional distribution $X|Y$ to be learned from data. We follow the approach in IGNN [Xu et al., 2022]. In this setting, the JKO-iFlow network pushes from the distribution $X|Y = k$ to the class-specific component in the Gaussian mixture of $H|Y = k$, see Figure A.8b and Appendix C.2.4 for more details. We apply JKO-iFlow to the Solar ramping dataset and compare it with the original IGNN model, and both models use graph neural network layers in the residual blocks. The results are shown in Figure A.9, where both the NLL and MMD-m metrics indicate the superior performance of JKO-iFlow and is consistent with the visual comparison.

6 Discussion

The work can be extended in several directions. The application to larger-scale image datasets and larger graphs will enlarge the scope of usage. To overcome the computational challenge faced by neural ODE models for high dimensional input, e.g., images of higher resolution, one would need to improve the training efficiency of the backpropagation in neural ODE in addition to the dimension reduction techniques by VAE as been explored here. Another possibility is to combine the JKO-iFlow scheme with other backbone flow models that are more suitable for the specific tasks. Meanwhile, it would be interesting to extend the method to other problems for which CNF models have proven to be effective. Examples include multi-dimensional probabilistic regression [Chen et al., 2018], a plug-in to deep architectures such as StyleFlow [Abdal et al., 2021], and the application to Mean-field Games [Huang et al., 2023].

References

Rameen Abdal, Peihao Zhu, Niloy J Mitra, and Peter Wonka. Styleflow: Attribute-conditioned exploration of stylegan-generated images using conditional continuous normalizing flows. *ACM Transactions on Graphics (ToG)*, 40(3):1–21, 2021.

Michael Samuel Albergo and Eric Vanden-Eijnden. Building normalizing flows with stochastic interpolants. In *The Eleventh International Conference on Learning Representations*, 2023.

David Alvarez-Melis, Yair Schiff, and Youssef Mroueh. Optimizing functionals on the space of probabilities with input convex neural networks. *Transactions on Machine Learning Research*, 2022. ISSN 2835-8856.

Brandon Amos, Lei Xu, and J Zico Kolter. Input convex neural networks. In *International Conference on Machine Learning*, pages 146–155. PMLR, 2017.

Miguel A Arcones and Evarist Gine. On the bootstrap of u and v statistics. *The Annals of Statistics*, pages 655–674, 1992.

Jens Behrmann, Will Grathwohl, Ricky TQ Chen, David Duvenaud, and Jörn-Henrik Jacobsen. Invertible residual networks. In *International Conference on Machine Learning*, pages 573–582. PMLR, 2019.

Adam Block, Youssef Mroueh, and Alexander Rakhlin. Generative modeling with denoising auto-encoders and langevin sampling. *arXiv preprint arXiv:2002.00107*, 2020.

Nicholas M Boffi and Eric Vanden-Eijnden. Probability flow solution of the fokker–planck equation. *Machine Learning: Science and Technology*, 4(3):035012, 2023.

François Bolley, Ivan Gentil, and Arnaud Guillin. Convergence to equilibrium in wasserstein distance for fokker–planck equations. *Journal of Functional Analysis*, 263(8):2430–2457, 2012.

Charlotte Bunne, Laetitia Papaxanthos, Andreas Krause, and Marco Cuturi. Proximal optimal transport modeling of population dynamics. In *International Conference on Artificial Intelligence and Statistics*, pages 6511–6528. PMLR, 2022.

Ricky TQ Chen, Yulia Rubanova, Jesse Bettencourt, and David K Duvenaud. Neural ordinary differential equations. *Advances in neural information processing systems*, 31, 2018.

Ricky TQ Chen, Jens Behrmann, David K Duvenaud, and Jörn-Henrik Jacobsen. Residual flows for invertible generative modeling. *Advances in Neural Information Processing Systems*, 32, 2019.

Michaël Defferrard, Xavier Bresson, and Pierre Vandergheynst. Convolutional neural networks on graphs with fast localized spectral filtering. *Advances in neural information processing systems*, 29, 2016.

Pierre Degond and S Mas-Gallic. The weighted particle method for convection-diffusion equations. i. the case of an isotropic viscosity. *Mathematics of computation*, 53(188):485–507, 1989.

Pierre Degond and Francisco-José Mustieles. A deterministic approximation of diffusion equations using particles. *SIAM Journal on Scientific and Statistical Computing*, 11(2):293–310, 1990.

Jia Deng, Wei Dong, Richard Socher, Li-Jia Li, Kai Li, and Li Fei-Fei. Imagenet: A large-scale hierarchical image database. In *2009 IEEE conference on computer vision and pattern recognition*, pages 248–255. Ieee, 2009.

Li Deng. The mnist database of handwritten digit images for machine learning research. *IEEE Signal Processing Magazine*, 29(6):141–142, 2012.

Laurent Dinh, David Krueger, and Yoshua Bengio. NICE: non-linear independent components estimation. In Yoshua Bengio and Yann LeCun, editors, *3rd International Conference on Learning Representations, ICLR 2015, San Diego, CA, USA, May 7-9, 2015, Workshop Track Proceedings*, 2015.

Laurent Dinh, Jascha Sohl-Dickstein, and Samy Bengio. Density estimation using real NVP. In *5th International Conference on Learning Representations, ICLR 2017, Toulon, France, April 24-26, 2017, Conference Track Proceedings*. OpenReview.net, 2017.

Patrick Esser, Robin Rombach, and Bjorn Ommer. Taming transformers for high-resolution image synthesis. In *Proceedings of the IEEE/CVF conference on computer vision and pattern recognition*, pages 12873–12883, 2021.

Jiaojiao Fan, Qinsheng Zhang, Amirhossein Taghvaei, and Yongxin Chen. Variational Wasserstein gradient flow. In *Proceedings of the 39th International Conference on Machine Learning*, pages 6185–6215. PMLR, 2022.

Matthias Fey and Jan E. Lenssen. Fast graph representation learning with PyTorch Geometric. In *ICLR Workshop on Representation Learning on Graphs and Manifolds*, 2019.

Chris Finlay, Jörn-Henrik Jacobsen, Levon Nurbekyan, and Adam Oberman. How to train your neural ode: the world of jacobian and kinetic regularization. In *International conference on machine learning*, pages 3154–3164. PMLR, 2020.

Ian J. Goodfellow, Jean Pouget-Abadie, Mehdi Mirza, Bing Xu, David Warde-Farley, Sherjil Ozair, Aaron C. Courville, and Yoshua Bengio. Generative adversarial nets. In *NIPS*, 2014.

Will Grathwohl, Ricky T. Q. Chen, Jesse Bettencourt, and David Duvenaud. Scalable reversible generative models with free-form continuous dynamics. In *International Conference on Learning Representations*, 2019.

Arthur Gretton, Karsten M. Borgwardt, Malte J. Rasch, Bernhard Schölkopf, and Alex Smola. A kernel two-sample test. *J. Mach. Learn. Res.*, 13:723–773, 2012a.

Arthur Gretton, Dino Sejdinovic, Heiko Strathmann, Sivaraman Balakrishnan, Massimiliano Pontil, Kenji Fukumizu, and Bharath K Sriperumbudur. Optimal kernel choice for large-scale two-sample tests. *Advances in neural information processing systems*, 25, 2012b.

Ishaan Gulrajani, Faruk Ahmed, Martín Arjovsky, Vincent Dumoulin, and Aaron C. Courville. Improved training of wasserstein gans. In *NIPS*, 2017.

Martin Heusel, Hubert Ramsauer, Thomas Unterthiner, Bernhard Nessler, and Sepp Hochreiter. Gans trained by a two time-scale update rule converge to a local nash equilibrium. *Advances in neural information processing systems*, 30, 2017.

Jonathan Ho, Ajay Jain, and Pieter Abbeel. Denoising diffusion probabilistic models. *Advances in Neural Information Processing Systems*, 33:6840–6851, 2020.

Chin-Wei Huang, Jae Hyun Lim, and Aaron C Courville. A variational perspective on diffusion-based generative models and score matching. *Advances in Neural Information Processing Systems*, 34: 22863–22876, 2021.

Han Huang, Jiajia Yu, Jie Chen, and Rongjie Lai. Bridging mean-field games and normalizing flows with trajectory regularization. *Journal of Computational Physics*, page 112155, 2023.

Michael F. Hutchinson. A stochastic estimator of the trace of the influence matrix for laplacian smoothing splines. *Communications in Statistics - Simulation and Computation*, 18:1059–1076, 1989.

Richard Jordan, David Kinderlehrer, and Felix Otto. The variational formulation of the fokker–planck equation. *SIAM journal on mathematical analysis*, 29(1):1–17, 1998.

Diederik P. Kingma and Jimmy Ba. Adam: A method for stochastic optimization. In Yoshua Bengio and Yann LeCun, editors, *3rd International Conference on Learning Representations, ICLR 2015, San Diego, CA, USA, May 7-9, 2015, Conference Track Proceedings*, 2015.

Diederik P. Kingma and Max Welling. Auto-encoding variational bayes. In Yoshua Bengio and Yann LeCun, editors, *2nd International Conference on Learning Representations, ICLR 2014, Banff, AB, Canada, April 14-16, 2014, Conference Track Proceedings*, 2014.

Diederik P. Kingma and Max Welling. An introduction to variational autoencoders. *Foundations and Trends® in Machine Learning*, 12(4):307–392, 2019.

Durk P Kingma and Prafulla Dhariwal. Glow: Generative flow with invertible 1x1 convolutions. *Advances in neural information processing systems*, 31, 2018.

Ivan Kobyzev, Simon JD Prince, and Marcus A Brubaker. Normalizing flows: An introduction and review of current methods. *IEEE transactions on pattern analysis and machine intelligence*, 43 (11):3964–3979, 2020.

Alexander Korotin, Vage Egiazarian, Arip Asadulaev, Alexander Safin, and Evgeny Burnaev. Wasserstein-2 generative networks. In *International Conference on Learning Representations*, 2021.

Alex Krizhevsky and Geoffrey Hinton. Learning multiple layers of features from tiny images. Technical Report 0, University of Toronto, Toronto, Ontario, 2009.

Yaron Lipman, Ricky T. Q. Chen, Heli Ben-Hamu, Maximilian Nickel, and Matthew Le. Flow matching for generative modeling. In *The Eleventh International Conference on Learning Representations*, 2023.

Jenny Liu, Aviral Kumar, Jimmy Ba, Jamie Kiros, and Kevin Swersky. Graph normalizing flows. *Advances in Neural Information Processing Systems*, 32, 2019.

Qiang Liu and Dilin Wang. Stein variational gradient descent: A general purpose bayesian inference algorithm. *Advances in neural information processing systems*, 29, 2016.

Emile Mathieu and Maximilian Nickel. Riemannian continuous normalizing flows. *Advances in Neural Information Processing Systems*, 33:2503–2515, 2020.

Petr Mokrov, Alexander Korotin, Lingxiao Li, Aude Genevay, Justin M Solomon, and Evgeny Burnaev. Large-scale wasserstein gradient flows. *Advances in Neural Information Processing Systems*, 34:15243–15256, 2021.

Derek Onken, S Wu Fung, Xingjian Li, and Lars Ruthotto. Ot-flow: Fast and accurate continuous normalizing flows via optimal transport. In *Proceedings of the AAAI Conference on Artificial Intelligence*, volume 35, 2021.

George Papamakarios, Theo Pavlakou, and Iain Murray. Masked autoregressive flow for density estimation. *Advances in neural information processing systems*, 30, 2017.

Adam Paszke, Sam Gross, Francisco Massa, Adam Lerer, James Bradbury, Gregory Chanan, Trevor Killeen, Zeming Lin, Natalia Gimelshein, Luca Antiga, Alban Desmaison, Andreas Kopf, Edward Yang, Zachary DeVito, Martin Raison, Alykhan Tejani, Sasank Chilamkurthy, Benoit Steiner, Lu Fang, Junjie Bai, and Soumith Chintala. Pytorch: An imperative style, high-performance deep learning library. In H. Wallach, H. Larochelle, A. Beygelzimer, F. d'Alché-Buc, E. Fox, and R. Garnett, editors, *Advances in Neural Information Processing Systems 32*, pages 8024–8035. Curran Associates, Inc., 2019.

Robin Rombach, Andreas Blattmann, Dominik Lorenz, Patrick Esser, and Björn Ommer. High-resolution image synthesis with latent diffusion models. In *Proceedings of the IEEE/CVF conference on computer vision and pattern recognition*, pages 10684–10695, 2022.

Litu Rout, Alexander Korotin, and Evgeny Burnaev. Generative modeling with optimal transport maps. In *International Conference on Learning Representations*, 2022.

Lars Ruthotto, Stanley J Osher, Wuchen Li, Levon Nurbekyan, and Samy Wu Fung. A machine learning framework for solving high-dimensional mean field game and mean field control problems. *Proceedings of the National Academy of Sciences*, 117(17):9183–9193, 2020.

Antonin Schrab, Ilmun Kim, MÃľlisande Albert, BÃľatrice Laurent, Benjamin Guedj, and Arthur Gretton. Mmd aggregated two-sample test. *Journal of Machine Learning Research*, 24(194):1–81, 2023.

Zebang Shen, Zhenfu Wang, Satyen Kale, Alejandro Ribeiro, Amin Karbasi, and Hamed Hassani. Self-consistency of the fokker planck equation. In *Conference on Learning Theory*, pages 817–841. PMLR, 2022.

Thomas C Sideris. *Ordinary differential equations and dynamical systems*, volume 2. Springer, 2013.

Karen Simonyan and Andrew Zisserman. Very deep convolutional networks for large-scale image recognition. In *International Conference on Learning Representations*, 2015.

Yang Song and Stefano Ermon. Generative modeling by estimating gradients of the data distribution. *Advances in Neural Information Processing Systems*, 32, 2019.

Yang Song, Jascha Sohl-Dickstein, Diederik P Kingma, Abhishek Kumar, Stefano Ermon, and Ben Poole. Score-based generative modeling through stochastic differential equations. In *International Conference on Learning Representations*, 2021.

Charles Stein. A bound for the error in the normal approximation to the distribution of a sum of dependent random variables. In *Proceedings of the sixth Berkeley symposium on mathematical statistics and probability, volume 2: Probability theory*, volume 6, pages 583–603. University of California Press, 1972.

Danica J. Sutherland, Hsiao-Yu Tung, Heiko Strathmann, Soumyajit De, Aaditya Ramdas, Alex Smola, and Arthur Gretton. Generative models and model criticism via optimized maximum mean discrepancy. In *International Conference on Learning Representations*, 2017.

Esteban G Tabak and Eric Vanden-Eijnden. Density estimation by dual ascent of the log-likelihood. *Communications in Mathematical Sciences*, 8(1):217–233, 2010.

Alexander Vidal, Samy Wu Fung, Luis Tenorio, Stanley Osher, and Levon Nurbekyan. Taming hyperparameter tuning in continuous normalizing flows using the jko scheme. *Scientific Reports*, 13(1):4501, 2023.

Chen Xu, Xiuyuan Cheng, and Yao Xie. Invertible neural networks for graph prediction. *IEEE Journal on Selected Areas in Information Theory*, 3(3):454–467, 2022.

Linfeng Zhang, Lei Wang, et al. Monge-Ampére flow for generative modeling. *arXiv preprint arXiv:1809.10188*, 2018.

Qinsheng Zhang and Yongxin Chen. Diffusion normalizing flow. *Advances in Neural Information Processing Systems*, 34:16280–16291, 2021.

A Proofs

A.1 Proofs in Section

Lemma A.1. *Suppose p and q are two densities on $\mathbb{R}^d$ in $\mathcal{P}$, the following two problems*

$$\min_{\rho\in\mathcal{P}} L_\rho[\rho] = \mathrm{KL}(\rho||q) + \frac{1}{2h}W_2^2(p,\rho), \tag{12}$$

$$\min_{T:\mathbb{R}^d\to\mathbb{R}^d} L_T[T] = \mathrm{KL}(T_\# p||q) + \frac{1}{2h}\mathbb{E}_{x\sim p}\|x - T(x)\|^2, \tag{13}$$

have the same minimum, and

(a) If $T^*:\mathbb{R}^d\to\mathbb{R}^d$ is a minimizer of (13)*, then $\rho^* = (T^*)_\# p$ is a minimizer of* (12)*.*

(b) If ρ^* is a minimizer of (12)*, then the optimal transport from p to ρ^* minimizes* (13)*.*

Proof of Lemma A.1. Let the minimum of (13) be L_T^*, and that of (12) be L_ρ^*.

Proof of (a): Suppose L_T achieves minimum at T^*, then T^* is the optimal transport from p to $\rho^* = (T^*)_\# p$ because otherwise L_T can be further improved. By definition of L_ρ, we have $L_T^* = L_T[T^*] = L_\rho[\rho^*] \geq L_\rho^*$. We claim that $L_T^* = L_\rho^*$. Otherwise, there is another ρ' such

that $L_\rho[\rho'] < L_T^*$. Let T' be the optimal transport from p to ρ', and then $L_T[T'] = L_\rho[\rho'] < L_T^*$, contradicting with that L_T^* is the minimum of L_T. This also shows that $L_\rho[\rho^*] = L_T^* = L_\rho^*$, that is, ρ^* is a minimizer of L_ρ.

Proof of (b): Suppose L_ρ achieves minimum at ρ^*. Let T^* be the OT from p to ρ^*, then $\mathbb{E}_{x\sim p}|x - T^*(x)|^2 = W_2(p, \rho^*)^2$, and then $L_T[T^*] = L_\rho[\rho^*] = L_\rho^*$ which equals L_T^* as proved in (a). This shows that T^* is a minimizer of L_T. □

Proof of Proposition 3.1, Given p_k being the density of $x(t)$ at $t = kh$, recall that T is the solution map from $x(t)$ to $x(t+h)$. We denote $\rho_t := p_k$, and $\rho_{t+h} := T_\# p_k$. By definition,

$$\mathrm{KL}(T_\# p_k || p_Z) = \mathbb{E}_{x\sim\rho_{t+h}}(\log \rho_{t+h}(x) - \log p_Z(x)). \tag{14}$$

Because $p_Z \propto e^{-V}$, $V(x) = |x|^2/2$, we have $\log p_Z(x) = -V(x) + c_1$ for some constant c_1. Thus

$$\mathbb{E}_{x\sim\rho_{t+h}} \log p_Z(x) = \mathbb{E}_{x(t)\sim\rho_t} \log p_Z(x(t+h)) = c_1 - \mathbb{E}_{x(t)\sim\rho_t} V(x(t+h)). \tag{15}$$

To compute the first term in (14), note that

$$\mathbb{E}_{x\sim\rho_{t+h}} \log \rho_{t+h}(x) = \mathbb{E}_{x(t)\sim\rho_t} \log \rho_{t+h}(x(t+h)), \tag{16}$$

and by the expression (called "instantaneous change-of-variable formula" in normalizing flow literature [Chen et al., 2018], which we derive directly in below)

$$\frac{d}{dt} \log \rho(x(t), t) = -\nabla \cdot \mathbf{f}(x(t), t), \tag{17}$$

we have that for each value of $x(t)$,

$$\log \rho_{t+h}(x(t+h)) = \log \rho(x(t+h), t+h) = \log \rho(x(t), t) - \int_t^{t+h} \nabla \cdot \mathbf{f}(x(s), s) ds.$$

Inserting back to (16), we have

$$\mathbb{E}_{x\sim\rho_{t+h}} \log \rho_{t+h}(x) = \mathbb{E}_{x(t)\sim\rho_t} \log \rho_t(x(t)) - \mathbb{E}_{x(t)\sim\rho_t} \int_t^{t+h} \nabla \cdot \mathbf{f}(x(s), s) ds).$$

The first term is determined by $\rho_t = p_k$, and thus is a constant c_2 independent from $\mathbf{f}(x, t)$ on $t \in [kh, (k+1)h]$. Together with (15), we have shown that

$$\text{r.h.s. of (14)} = c_2 - \mathbb{E}_{x(t)\sim\rho_t} \int_t^{t+h} \nabla \cdot \mathbf{f}(x(s), s) ds) - c_1 + \mathbb{E}_{x(t)\sim\rho_t} V(x(t+h)),$$

which proves (7).

Derivation of (17): by chain rule,

$$\begin{aligned}
\frac{d}{dt} \log \rho(x(t), t) &= \frac{\nabla \rho(x(t), t) \cdot \dot{x}(t) + \partial_t \rho(x(t), t)}{\rho(x(t), t)} \\
&= \left. \frac{\nabla \rho \cdot \mathbf{f} - \nabla \cdot (\rho \mathbf{f})}{\rho} \right|_{(x(t),t)} \quad \text{(by (1) and (2))} \\
&= -\nabla \cdot \mathbf{f}(x(t), t).
\end{aligned}$$

□

B Technical details of Section 4

To train the proposed JKO-iFlow model by Algorithm 1, one needs to specify a sequence of t_k, where the k-th JKO block integrates from t_{k-1} to t_k, starting from $t_0 = 0$. Denote by $h_k := t_{k+1} - t_k$ the step-size for k-th step.

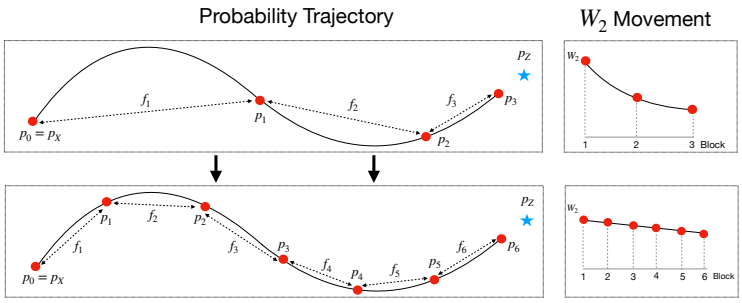

Figure A.1: Diagram illustrating trajectory reparameterization and refinement. Top: the original trajectory under three blocks via Algorithm 1. Bottom: the trajectory under six blocks after reparameterization and refinement, which renders the W2 movements more even.

B.1 Initial choice of t_k in Algorithm 1

We first initialize the choice by the following scheme

$$h_k = \min\{\rho^k h_0, h_{\max}\}, \quad k = 0, 1, \cdots \tag{18}$$

where the base stepsize h_0, the multiplying factor $\rho \geq 1$, and the maximum stepsize $h_{\max} \geq h_0$ are three hyper-parameters to be specified by the user. When $\rho = 1$, the sequence of h_k in (18) corresponds to constant stepsize $h_k \equiv h_0$.

Applying Algorithm 1 with the initial choice of t_k gives L trained residual blocks of the neural ODE model, where L is to be determined by the stopping criterion in Section 4.1. The model is further improved by the two additional techniques in Section 4.2, which will adaptively specify the stepsize h_k and we explain in detail below.

B.2 Hutchinson trace via finite difference

We propose a finite-difference estimator of $\nabla \cdot \mathbf{f}(x,t) = \mathrm{Tr}(J_{\mathbf{f}}(x))$, where $J_{\mathbf{f}}(x))$ is the Jacobian of $\mathbf{f}$ at x. This is based on the Hutchinson trace estimator [Hutchinson, 1989], which states that $\mathrm{Tr}(J_{\mathbf{f}}(x)) = \mathbb{E}_{p(\epsilon)}\left[\epsilon^T J_{\mathbf{f}}(x)\epsilon\right]$. Here, $p(\epsilon)$ is a distribution in $\mathbb{R}^d$ satisfying $\mathbb{E}[\epsilon] = 0$ and $\mathrm{Cov}(\epsilon) = I$ (e.g., a standard Gaussian). Existing CNF works estimate the expectation by sampling $\epsilon \sim p(\epsilon)$ and computing the vector-Jacobian product $J_{\mathbf{f}}(x)\epsilon$ using reverse-mode automatic differentiation. The product $J_{\mathbf{f}}(x)\epsilon$ can be computed for approximately the same cost as evaluating $\mathbf{f}$ [Grathwohl et al., 2019].

Now, given a fixed ϵ, we have $J_{\mathbf{f}}(x)\epsilon = \lim_{\sigma\to 0} \frac{\mathbf{f}(x+\sigma\epsilon)-\mathbf{f}(x)}{\sigma}$, which is the directional derivative of $\mathbf{f}$ along the direction ϵ. Thus, given a fixed small $\sigma > 0$, we propose the following finite-difference estimator of $\nabla \cdot \mathbf{f}(x,t)$:

$$\nabla \cdot \mathbf{f}(x,t) \approx \mathbb{E}_{p(\epsilon)}\left[\epsilon^T \frac{\mathbf{f}(x+\sigma\epsilon) - \mathbf{f}(x)}{\sigma}\right]. \tag{19}$$

The finite-difference approximation of $J_{\mathbf{f}}(x)\epsilon$ requires only one additional function evaluation of $\mathbf{f}$ at $x + \sigma\epsilon$ and avoids the computation of automatic differentiation. We empirically found that training with (19) on high-dimensional examples (e.g., $d > 100$ as in image examples) can be approximately 1.5$\sim$2 times faster than existing CNF approaches relying on reverse-mode automatic differentiation. In all experiments, we let $\sigma = \sigma_0/\sqrt{d}$ with $\sigma_0 = 0.02$.

B.3 Trajectory improvement illustrated in vector space

Section 4.2 introduces two techniques to improve the computation of a gradient descent trajectory represented by discrete points. For illustrative purposes, we introduce the two techniques when the gradient system is in a vector space equipped with Euclidean metric. The JKO-iFlow training applies the same technique in the gradient system equipped with the Wasserstein-2 metric.

Let the space be $\mathbb{R}^d$, and $F : \mathbb{R}^d \to \mathbb{R}$ be a differential landscape. Given a sequence of positive stepsize h_k, one can compute a sequence of representative points x_k which discretizes the gradient

descent trajectory of minimizing F (towards a local minimum x^*). Specifically, we have

$$x_{k+1} = \arg\min_x F(x) + \frac{1}{2h_k}\|x - x_k\|_2^2, \tag{20}$$

starting from some fixed x_0.

B.3.1 Trajectory reparameterization

Starting from an initial sequence of step-size $\{h_k\}_{k=1}^L$ as in Section B.1, the reparameterization technique implements an iterative scheme to update the sequence of h_k adaptively. We call the j-th iteration 'Iter-j', and denote the sequence by $\{h_k^{(j)}\}_{k=1}^L$. The corresponding solution points x_k by solving (20) with $h_k^{(j)}$ are denoted as $x_k^{(j)}$. In addition to the constant $h_{\max}$, we need another algorithmic parameter $\eta \in (0, 1)$, and we set $\eta = 0.3$ for the vector-space example in computation.

We always have $x_0^{(j)} = x_0$ for all 'Iter-j'. In the j-th iteration of the parametrization, we compute the following

1. Compute the *arclength* as
$$S_k^{(j)} := \|x_{k-1}^{(j)} - x_k^{(j)}\|_2, \quad k = 1, \cdots, L. \tag{21}$$
2. Compute the average arclength
$$\bar{S} := \sum_{k=1}^{L} S_k^{(j)}/L.$$
3. Update the stepsize for $k = 1, \ldots, L$ as
$$h_k^{(j+1)} := \min\{h_k^{(j)} + \eta(\bar{S}h_k^{(j)}/S_k^{(j)} - h_k^{(j)}), h_{\max}\}$$
4. Solve (20) using $h_k^{(j+1)}$ to obtain $x_k^{(j+1)}$.

We terminate the iteration when the arclengths $\{S_k^{(j)}\}$ are approximately equal. An illustration is given as Iter-12 in the upper panel of Figure A.2. After the reparameterization iterations, we solve an additional x_{L+1} by minimizing $F(x)$ starting from x_L. This corresponds to optimizing the "free-block" in Algorithm 1.

B.3.2 Progressive refinement

The scheme can be computed using a positive integer refinement factor. For simplicity, we use factor 2 throughout this work.

Given a sequence of $\{h_k\}_{k=1}^L$ and the representitive points $\{x_k\}_{k=1}^L$, the refinement scheme computes a refined trajectory having $k = 1, \cdots, 2L$:

1. Compute the refined stepsizes as
$$\tilde{h}_{2k-1} = \tilde{h}_{2k} = h_k/2, \quad k = 1, \ldots, L$$
2. Compute the representative points $\tilde{x}_k$ by solving (20) using $\tilde{h}_k$, possibly warm-starting by $\tilde{x}_{2k} = x_k$ and $\tilde{x}_{2k-1} = (x_k + x_{k-1})/2$.

We then apply the trajectory reparameterization iterations as in Section B.3.1 to the refined trajectory till convergence, and the free-block ending point is also recomputed. An illustration is given as r-Iter-10 in the upper panel of Figure A.2.

B.4 Trajectory improvement in probability space

We apply the two techniques to solve the JKO step (8), which is the counterpart of (20) as a gradient descent scheme with proximal steps. The representative points x_k are replaced with transported distributions p_k which form a sequence of points in $\mathcal{P}$, and the optimization is over the parametrization of p_k induced by the neural network flow mapping consisting of the first k residual blocks.

It remains to define the arclength in (21) to implement the two techniques. Because we equip $\mathcal{P}$ with the Wasserstein-2 metric, we compute (omitting the iteration index j in the notation)

$$S_k = W_2(p_{k-1}, p_k) = (\mathbb{E}_{x\sim p_{k-1}} \|x - T_k(x)\|^2)^{1/2}, \tag{22}$$

where the transport mapping $T_k(x) = x + \int_{t_{k-1}}^{t_k} f_{\theta_k}(x(s), s)ds$ and can be computed from the k-th block. In practice, the expectation $\mathbb{E}_{x\sim p_{k-1}}$ in (22) is computed by a finite-sample average on the training set.

At last, the optimal warm-start of p_k in the refinement is implemented by inheriting the parameters θ_k of the trained blocks.

C Experimental details

C.1 Quantitative evaluation metrics

Besides visual comparison, we adopt two quantitative metrics to evaluate the performance of generative models, the negative log-likelihood (NLL) metric Grathwohl et al. [2019] and the maximum mean discrepancy (MMD) [Gretton et al., 2012a] metric.

C.1.1 NLL metric

Our computation of the NLL metric follows the standard procedure for neural ODE normalizing flow models Chen et al. [2018], Grathwohl et al. [2019], where the evolution of density $\rho(x(t))$ can be computed via integrating $\nabla \cdot \mathbf{f}(x(t), t)$ over time due to the instantaneous change-of-variable formula (17).

Specifically, our model flows from $t_0 = 0$ to $t_{L+1} = T$, where $x(0) \sim p_0$ the data distribution, and we train the flow model to make $x(T)$ follow a normal density q. The model density at data sample x

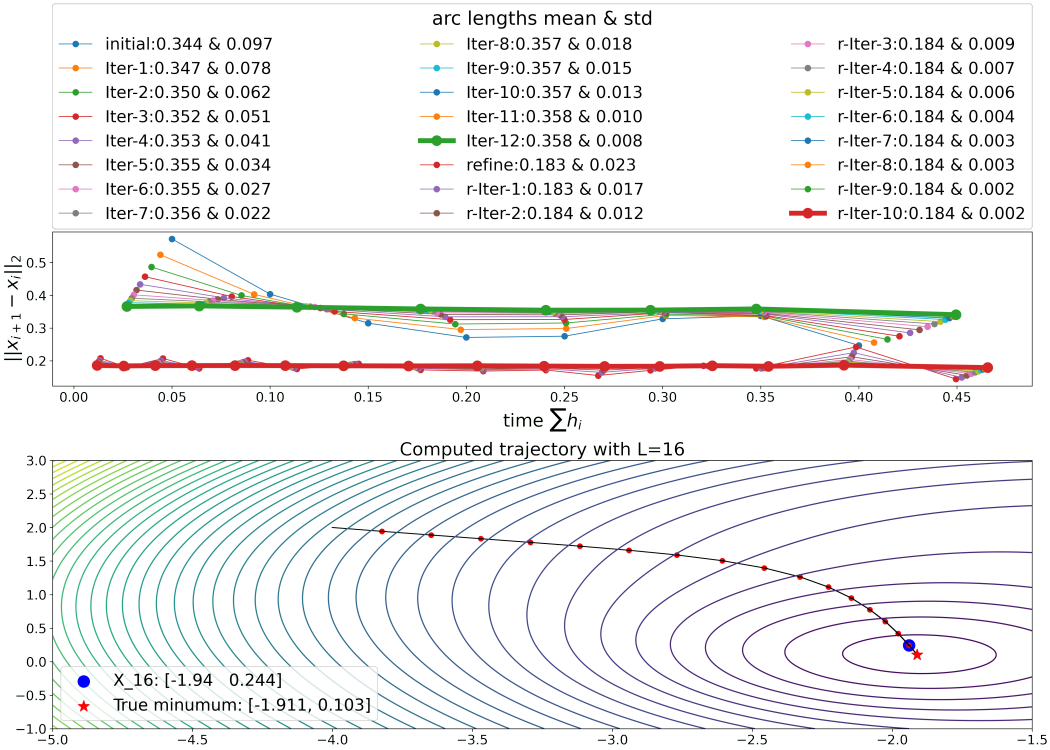

Figure A.2: The upper panel shows the arc lengths and the mean and standard deviation of arc lengths over 12 reparameterization iterations, one refinement, and an additional 10 reparameterization iterations. The lower panel visualizes the trajectory consisting of 17 solution points at "r-Iter-10", where the free point as the 17-th point computes the appproximate minimum by $x_{17} = x_{L+1} = [-1.911, 0.105]$.

is expressed as $\rho(x,0) = (T_\theta^{-1})_\# q(x)$ where T_θ^{-1} is the inverse model flow mapping from $x(T)$ to $x(0)$. Thus the model log-likelihood can be expressed as

$$\log \rho(x(0),0) = \log q(x(T),T) + \int_0^T \nabla \cdot \mathbf{f}(x(s),s)ds.$$

In practice, our trained flow model has L blocks where each block f_{θ_k} represents $\mathbf{f}(x,t)$ on $[t_{k-1}, t_k)$ and is parametrized by θ_k. The log-likelihood at test sample x is then computed by

$$\mathrm{LL}(x) = -\frac{1}{2}(\|x(t_{L+1})\|_2^2 + d\log(2\pi)) + \sum_{k=1}^{L+1} \int_{t_{k-1}}^{t_k} \nabla \cdot f_{\theta_k}(x(s),s)ds, \tag{23}$$

where

$$x(t_k) = x(t_{k-1}) + \int_{t_{k-1}}^{t_k} f_{\theta_k}(x(s),s)ds$$

starting from $x(0) = x$. Both the integration of f_{θ_k} and $\nabla \cdot f_{\theta_k}$ are computed using the numerical scheme of neural ODE. We report NLL in the natural unit of information (i.e., $\log$ with base e, known as "nats") in all our experiments.

C.1.2 MMD metrics

Note that the normalizing flow models use NLL (on training set) as the training objective. In contrast, the MMD metric is an impartial evaluation metric as it is not used to train JKO-iFlow or any competing methods. Given two set of data samples $\boldsymbol{X} := \{x_i\}_{i=1}^N$ and $\tilde{\boldsymbol{X}} := \{\tilde{x}_j\}_{j=1}^M$ and a kernel function $k(x,\tilde{x})$, the (squared) kernel MMD [Gretton et al., 2012a] is defined as

$$\mathrm{MMD}(\boldsymbol{X},\tilde{\boldsymbol{X}}) := \frac{1}{N^2}\sum_{i=1}^N\sum_{j=1}^N k(x_i,x_j) + \frac{1}{M^2}\sum_{i=1}^M\sum_{j=1}^M k(\tilde{x}_i,\tilde{x}_j) - \frac{2}{NM}\sum_{i=1}^N\sum_{j=1}^M k(x_i,\tilde{x}_j), \tag{24}$$

When a generative model is trained, we generate M i.i.d. data samples by the model to construct the set $\tilde{\boldsymbol{X}}$, and we form the set $\boldsymbol{X}$ using N true data samples (from the test set). MMD metrics with other choices of kernels are possible Gretton et al. [2012b], Sutherland et al. [2017], Schrab et al. [2023]. In all experiments here, we use the Gaussian kernel $k(x,\tilde{x}) = \exp\{-\|x-\tilde{x}\|^2/2h^2\}$ to stay consistent with reported baselines from [Onken et al., 2021], where $h > 0$ is the bandwidth parameter. We use three ways of setting the bandwidth parameter h:

- Constant bandwidth: $h = h_c = 1$. The resulting MMD is denoted as 'MMD-1'.
- Median bandwidth [Gretton et al., 2012a]: let $h = h_m$ be the median of $\|x_i - x_j\|$ for all distinct i and j. The median distance is computed from the dataset X. The resulting MMD is denoted as 'MMD-m'.
- Custom bandwidth: on certain datasets when we can use prior knowledge to decide on the bandwidth, we will custom the choice of h (typically smaller than the median distance, due to that theoretically smaller bandwidth may lead to a more powerful MMD test to distinguish the difference in the underlying distributions) while ensuring that we use large enough M and N to compute the MMD metric. We call the metric 'MMD-c'.

On all datasets, we use at most $N = 10K$ test samples as $\mathbf{X}$, and for each trained model, we generate $M = 10K$ test samples to form the dataset $\tilde{\mathbf{X}}$ to compute the MMD value defined as in (24). Note that the MMD metric as a measure of distance between two distributions is significant when above a test threshold τ, which is defined as the upper $(1-\alpha)$-quantile of the distribution of the MMD statistic under the null hypothesis (i.e., when dataset $\mathbf{X}$ and $\tilde{\mathbf{X}}$ observe the same distribution). The scalar α is the controlled Type-I error (known as the test level), which is set to be 0.05. To obtain the test threshold τ for the MMD, we adopt the bootstrap procedure Arcones and Gine [1992], Gretton et al. [2012a] and compute τ as the empirical $(1-\alpha)$-quantile of the simulated null distribution of the MMD from the pool of samples formed by the union of $\mathbf{X}$ and $\tilde{\mathbf{X}}$, where the set $\tilde{\mathbf{X}}$ is generated by the trained JKO-iFlow model. We use 1000 times of bootstrap in all experiments. In our usage of evaluating generative models, the threshold τ can be viewed a baseline of the MMD metric, that is, when the computed MMD values are above τ, then the smaller the MMD value the better the generative performance; when the computed MMD value is below τ, it means that with respect to the current MMD metric, the trained model generates a data distribution that is as good as the true distribution.

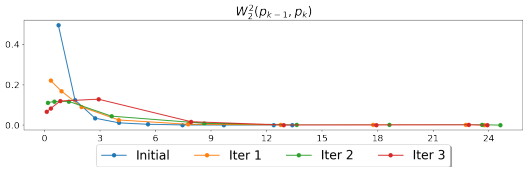

(a) Per-block W_2^2 over reparameterization iterations.

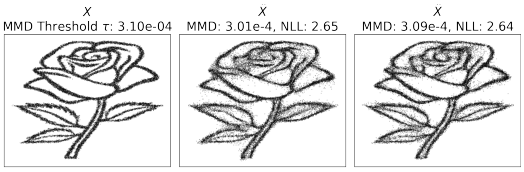

(b) Results at initial training (middle) and Iter 3 (right). MMD and NLL values are shown in the title.

Figure A.3: Same plots as in Figure A.5 for Rose data. We observe improved generative quality on the leaves of the rose after reparameterization iterations

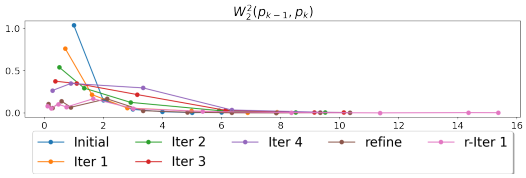

(a) Per-block W_2^2 over reparameterization iterations and refinement ('r-Iter 1' means one reparameterization iteration after refinement).

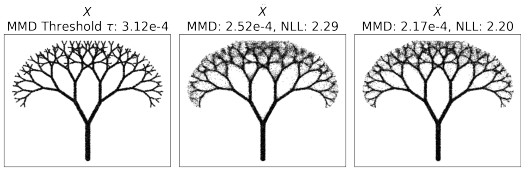

(b) Results at Iter 4 (middle) and r-Iter 1 (right). MMD and NLL values are shown in the title.

Figure A.4: Same plots as in Figure A.5 for Fractal tree data. We observe improved generative quality on the edges of the tree after refinement.

C.2 Detail setup and additional results

All experiments are conducted using PyTorch [Paszke et al., 2019] and PyTorch Geometric [Fey and Lenssen, 2019]. The optimizer is Adam [Kingma and Ba, 2015] with learning rates to be specified in each example. We use the neural-ODE integrator [Grathwohl et al., 2019, adjoint method] on two-dimensional examples and image examples, and use back-propagation on all other examples.

C.2.1 Two-dimensional toy data

Training and test data: We generate 8K test samples for each dataset, and for the training split,

- For Rose (Figure 2 and A.3) and Checkerboard and Olympic rings (Figure 2), we re-sample 10K training samples every epoch, for a total of 100 epochs per block. The batch size is 500.
- For Fractal tree (Figure 2 and A.4), we use a fixed training data of 200K samples, for a total of 50 epochs per block. The batch size is 2000.

Choice of h_k: The initial schedule is by setting $h_0 = 0.75, \rho = 1.2$. We set $h_{\max} = 5$ for rose, checkerboard, and Olympic rings, and $h_{\max} = 3$ for fractal tree. For reparametrization and refinement, we use $\eta = 0.5$ in the reparameterization iterations for all examples.

- For Rose, 3 reparameterization moving iteration, no refinement.
- For Checkerboard and Olympic rings, 4 reparameterization moving iteration, no refinement.
- For Fractal tree, 4 reparameterization moving iteration, one refinement, and an additional reparameterization moving iteration.

MMD metric: We use custom kernel bandwidth $h = 0.1h_m$ where h_m is the median distance of dataset $\mathbf{X}$ with $N = 8K$ (from true data distribution). From trained generative model, we generate $M = 10K$ test samples as $\tilde{\mathbf{X}}$.

Network and activation: Fully-connected residual blocks with two hidden layers. We use the softplus activation ($\beta = 20$) with 128 hidden dimension. Before refinement, we train 9 residual blocks for

Table A.1: Inversion error $\mathbb{E}_{x\sim p_X} \|T_\theta^{-1}(T_\theta(x)) - x\|_2^2$ of JKO-iFlow computed via sample average on the test split of the data set, where T_θ denotes the transport mapping over all the blocks of the trained flow network.

Rose	Fractal tree	Olympic rings	Checkerboard	POWER	GAS	MINIBOONE	BSD300	MNIST
3.30e-6	3.58e-5	2.24e-6	3.07e-5	1.48e-5	1.58e-6	1.09e-6	1.53e-5	1.87e-5

Table A.2: Complete results on real tabular datasets to augment Table 1 under the fixed-budget setting. L denotes to the number of residual blocks used in each dataset; for comparison, the free block in JKO-iFlow is not used. For fair comparison across models, the number of batches indicates how many batches pass through all residual blocks.

Data Set	Model	# Param	Training				Testing		
			Time (h)	# Batches	Time/Batches (s)	Batch size	MMD-m	MMD-1	NLL
							τ: **1.73e-4**	τ: **2.90e-4**	
POWER $d = 6$	JKO-iFlow	76K, L=4	0.07	0.76K	3.51e-1	10000	9.86e-5	2.40e-4	-0.12
	OT-Flow	76K	0.36	7.58K	1.71e-1	10000	7.58e-4	5.35e-4	0.32
	FFJORD	76K, L=4	0.67	7.58K	3.18e-1	10000	9.89e-4	1.16e-3	0.63
	IGNN	304K, L=16	0.29	7.58K	1.38e-1	10000	1.93e-3	1.59e-3	0.95
	IResNet	304K, L=16	0.41	7.58K	1.95e-1	10000	3.92e-3	2.43e-2	3.37
	ScoreSDE	76K	0.06	7.58K	2.85e-2	10000	9.12e-4	6.08e-3	3.41
	ScoreSDE	76K	0.60	75.80K	2.85e-2	10000	7.12e-4	5.04e-3	3.33
	JKO-iFlow	57K, L=3	0.05	0.76K	2.63e-1	10000	3.86e-4	7.20e-4	-0.06
							τ: **1.85e-4**	τ: **2.73e-4**	
GAS $d = 8$	JKO-iFlow	76K, L=4	0.07	0.76K	3.32e-1	5000	1.52e-4	5.00e-4	-7.65
	OT-Flow	76K	0.23	7.60K	1.09e-1	5000	1.99e-4	5.16e-4	-6.04
	FFJORD	76K, L=4	0.65	7.60K	3.08e-1	5000	1.87e-3	3.28e-3	-2.65
	IGNN	304K, L=16	0.34	7.60K	1.61e-1	5000	6.74e-3	1.43e-2	-1.65
	IResNet	304K, L=16	0.46	7.60K	2.18e-1	5000	3.20e-3	2.73e-2	-1.17
	ScoreSDE	76K	0.03	7.60K	1.42e-2	5000	1.05e-3	8.36e-4	-3.69
	ScoreSDE	76K	0.30	76.00K	1.42e-2	5000	2.23e-4	3.38e-4	-5.58
	JKO-iFlow	95K, L=5	0.09	0.76K	4.15e-1	5000	1.51e-4	3.77e-4	-7.80
							τ: **2.46e-4**	τ: **3.75e-4**	
MINIBOONE $d = 43$	JKO-iFlow	112K, L=4	0.03	0.34K	3.61e-1	2000	9.66e-4	3.79e-4	12.55
	OT-Flow	112K	0.21	3.39K	2.23e-1	2000	6.58e-4	3.79e-4	11.44
	FFJORD	112K, L=4	0.28	3.39K	2.97e-1	2000	3.51e-3	4.12e-4	23.77
	IGNN	448K, L=16	0.63	3.39K	6.69e-1	2000	1.21e-2	4.01e-4	26.45
	IResNet	448K, L=16	0.71	3.39K	7.54e-1	2000	2.13e-3	4.16e-4	22.36
	ScoreSDE	112K	0.01	3.39K	6.37e-3	2000	5.86e-1	4.33e-4	27.38
	ScoreSDE	112K	0.10	33.90K	6.37e-3	2000	4.17e-3	3.87e-4	20.70
							τ: **1.38e-4**	τ: **1.01e-4**	
BSDS300 $d = 63$	JKO-iFlow	396K, L=4	0.05	1.03K	1.85e-1	1000	2.24e-4	1.91e-4	-153.82
	OT-Flow	396K	0.62	10.29K	2.17e-1	1000	5.43e-1	6.49e-1	-104.62
	FFJORD	396K, L=4	0.54	10.29K	1.89e-1	1000	5.60e-1	6.76e-1	-37.80
	IGNN	990K, L=10	1.71	10.29K	5.98e-1	1000	5.64e-1	6.86e-1	-37.68
	IResNet	990K, L=10	2.05	10.29K	7.17e-1	1000	5.50e-1	5.50e-1	-33.11
	ScoreSDE	396K	0.01	10.29K	3.50e-3	1000	5.61e-1	6.60e-1	-7.55
	ScoreSDE	396K	0.10	102.90K	3.50e-3	1000	5.61e-1	6.62e-1	-7.31
	JKO-iFlow	396K, L=4	0.08	1.03K	2.76e-1	5000	1.41e-4	8.83e-5	-156.68

rose, checkerboard, and Olympic rings, and train 6 residual blocks for fractal trees. Learning rate is 5e-3.

Additional results: Figure A.3 and A.4 illustrates the benefits of reparameterization and refinement. Specifically, the details of the generated rose around portions of leaves and of the generated tree around smallest edges are clearer using these techniques. In terms of quantitative metrics, the NLL is also smaller, even though the MMD metric indicates there is no statistical difference between the ground truth and generated samples.

C.2.2 Tabular datasets

Training and test data: The four high-dimensional real datasets (POWER, GAS, MINIBOONE, BSDS300) come from the University of California Irvine (UCI) machine learning data repository, and we follow the pre-processing procedures of [Papamakarios et al., 2017]. Regarding data sizes,

- POWER: 1.85M training sample and 205K test sample.
- GAS: 1M training sample, 100K test sample.
- MINIBOONE: 32K training sample, 3.6K test sample.
- BSDS300: 1.05M training sample, 250K test sample.

Choice of h_k: The initial schedule is by setting $h_0 = 1, \rho = 1, h_{\max} = 3$. For reparametrization and refinement, we use $\eta = 0.5$ in the reparameterization iterations for all datasets.

MMD metric: When the test data from the MINIBOONE dataset is less than 10K in size, we use all the test set as $\mathbf{X}$ and N is the size of test data. When the test data from all three other datasets has more than 10K samples, we randomly select $N = 10K$ samples from the entire test data, and the same random test subset is used to evaluate all models. We use the median distance kernel bandwidth and generate $M = 10K$ test samples from each model to form $\tilde{\mathbf{X}}$.

Network and activation: We use the Tanh activation for all networks. Regarding design of residual blocks, we use fully-connected residual blocks with two hidden layers. On POWER, GAS, and MINIBOONE, we use 128 hidden nodes, and on BSDS300, we use 256 hidden nodes. The number of residual blocks for four tabular datasets is described in Tables A.2 and A.4. Regarding learning rate, it is 1e-3 on POWER, 2e-3 on GAS, 5e-3 on MINIBOONE, and 1.75e-3 on BSDS300.

Additional results: For experiments under the fixed-budget setting, Table A.2 shows the complete results of JKO-iFlow against competitors on tabular datasets. In the extra lines in the table, we show the result of JKO-iFlow with L=3 for POWER and L=5 for GAS, as these numbers of L are determined by the termination criterion in Algorithm 1. (The main lines show the results with $L = 4$ so that our model has the same capacity with the alternatives.) BSDS300 has an extra line for JKO-iFlow trained with batch sizes 5000, which improves over the result with batch size 1000. The baseline models FFJORD, IGNN, and IResNet are trained end-to-end, and as a result cannot afford the larger batch size on this example due to GPU memory constraints. For ScoreSDE, we use the implementation in [Huang et al., 2021], which computes the evidence lower bound (ELBO) for the data log-likelihood as reported in the last column. Although ScoreSDE is the fastest, its performance, even under 100 times more mini-batch stochastic gradient descent steps than JKO-iFlow, is still worse than JKO-iFlow in terms of both MMD-m and NLL. To ensure a fair comparison against diffusion models, we perform additional experiments of using different noise schedulers $\beta(t)$ and $\bar{\beta}_{\max}$ in ScoreSDE on MINIBOONE, following the noise scheduler suggestions in DDPM [Ho et al., 2020]. Note that DDPM can be viewed as a discrete-time version of the variance-preserving ScoreSDE model. As shown in Table A.3, the performance of ScoreSDE is indeed sensitive to the noise schedule. However, the best NLL of ScoreSDE 17.45 from the table is still noticeably higher than the NLL of 12.55 obtained by JKO-iFlow on MINIBOONE in Table A.2, and JKO-iFlow is trained using ten times less number of batches. To visualize the generative performance, scatter plots of the generated samples by JKO-iFlow and competitors on these tabular datasets are shown in Figure A.6 after projected to 2 dimensions (determined by principal components computed from true data test samples). The plots show a closer match between those from JKO-iFlow with the ground truth in distribution.

For experiments allowing more expensive models and longer training time, Table A.4 shows the results of JKO-iFlow after additional training of trajectory reparametrization in comparison with other baselines cited from the original papers. We run 7 reparameterization iterations on POWER, GAS, and MINIBOONE and 1 reparametrization iteration on BSDS300. A free block is used on POWER, GAS, and BSDS300.

C.2.3 Image generation with pre-trained variational auto-encoder

We perform image generation on MNIST [Deng, 2012], CIFAR10 [Krizhevsky and Hinton, 2009], and Imagenet-32 [Deng et al., 2009] datasets. We do so in the latent space of a pre-trained VAE, where we discuss the details below.

Table A.3: NLL per noise scheduler and $\bar{\beta}_{\max}$ combination of ScoreSDE on MINIBOONE. The three settings "linear, constant, quadratic" follow the DDPM suggestion [Ho et al., 2020]. The mean and standard deviation are computed over three replicas of the trained model.

Noise scheduler \ $\bar{\beta}_{\max}$	1	5	10	15	20
Linear	24.51 (0.24)	18.73 (0.64)	20.28 (0.38)	26.76 (1.77)	26.83 (1.23)
Constant	25.47 (0.25)	30.37 (0.84)	37.73 (0.98)	40.47 (1.27)	45.32 (0.40)
Quadratic	27.19 (0.14)	17.45 (0.17)	18.48 (0.38)	18.90 (0.48)	21.35 (0.60)

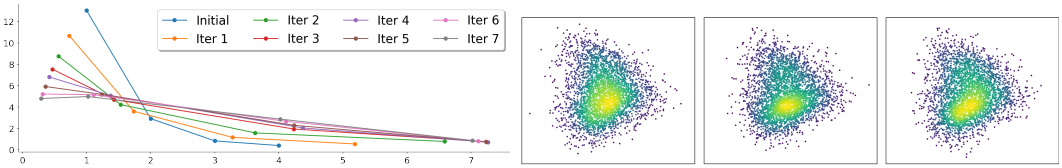

(a) Per-block W_2^2 over reparameterization iterations.

(b) Results at initial training (middle) and Iter 7 (right).

Figure A.5: Reparametrization iterations of JKO-iFlow model on MINIBOONE. (a) After 7 reparameterization iterations, a trajectory of more uniform W_2 movements is obtained. (b) Generated samples by the models before and after the moving iterations (visualized in the first two principal components computed from test data).

Table A.4: The OT-Flow and FFJORD baselines marked with * are from the original papers [Onken et al., 2021] and [Grathwohl et al., 2019]. The results of JKO-iFlow are obtained after applying the reparameterization technique.

Data Set	Model	# Param	Training		Testing
			# Batches	Batch size	NLL
POWER $d = 6$	JKO-iFlow	95K, L=5	6.08K	10000	-0.40
	OT-Flow*	18K	22K	10000	-0.30
	FFJORD*	43K, L=5	-	10000	-0.46
GAS $d = 8$	JKO-iFlow	114K, L=6	6.08K	5000	-9.43
	OT-Flow*	127K	52K	2000	-9.20
	FFJORD*	279K, L=5	-	1000	-8.59
MINIBOONE $d = 43$	JKO-iFlow	112K, L=4	2.72K	2000	10.55
	OT-Flow*	78K	7K	2000	10.55
	FFJORD*	821K, L=1	-	1000	10.43
BSDS300 $d = 63$	JKO-iFlow	495K, L=5	2.06K	5000	-157.75
	OT-Flow*	297K	37K	300	-154.20
	FFJORD*	6.7M, L=2	-	10000	-157.40

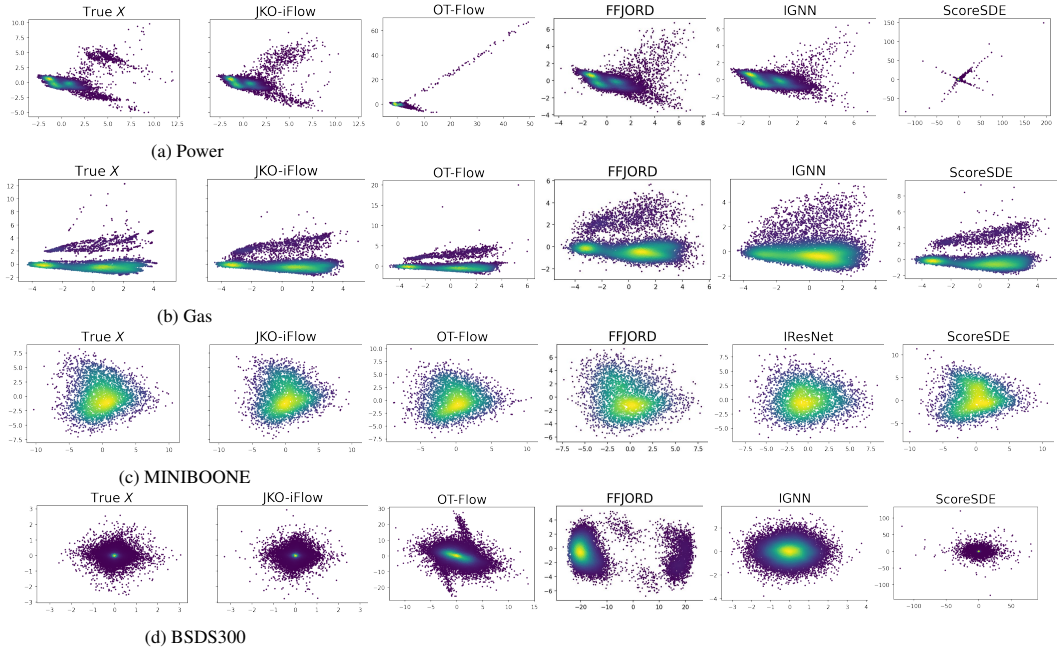

Figure A.6: Generative quality on tabular datasets via PCA projection of generated samples. The generative quality in general aligns with the quantitative metrics in Table 1 and A.2.

VAE as data pre-processing: We train deep VAEs in an adversarial manner following [Esser et al., 2021], and use pre-trained VAEs to pre-process the input images X. Specifically, the encoder $\mathcal{E} : X \to (\mu(X), \Sigma(X))$ of the VAE maps a RGB-image X to parameters of a multivariate Gaussian distribution $\mathcal{N}(\mu(X), \Sigma(X))$ in a lower dimension $\tilde{d}$. Then, given any random latent code $\tilde{X} \sim \mathcal{N}(\mu(X), \Sigma(X))$, the decoder $\mathcal{D} : \tilde{X} \to \hat{X}$ of the VAE is trained so that $X \approx \hat{X}$ for the reconstructed image $\hat{X} = \mathcal{D}(\tilde{X})$. On MNIST, we let the latent-space dimension $\tilde{d} = 20$, and on CIFAR10 and ImageNet32, we let the latent-space dimension $\tilde{d} = 192$. There are 5.6M parameters in the VAE encoder and 8.25M parameters in the VAE decoder. Given a trained VAE, we then train the JKO-iFlow model T_θ to transport invertibly between the distribution of random latent codes $\tilde{X}$ defined over all training images X and the standard multivariate Gaussian distribution in $\mathbb{R}^{\tilde{d}}$.

Training and test data: Training data: 60K images in MNIST, 50K images in CIFAR10, and 1.28M images in Imagenet-32. Test data: 10K images in MNIST and CIFAR10, and 50K images in Imagenet-32.

Choice of h_k: on MNIST, we specify $\{h_0 = 1, \rho = 1, h_{\max} = 1\}$. on CIFAR10, we specify $\{h_0 = 1, \rho = 1, h_{\max} = 1\}$. On Imagenet-32, we specify $\{h_0 = 1, \rho = 1.1, h_{\max} = \infty\}$. We train

$L = 6$ blocks on MNIST, and we train $L = 8$ blocks on CIFAR10 and Imagenet-32. On CIFAR10 and Imagenet-32, we also scale $h_k = T \cdot h_k / \sum_j h_j$ so $\sum_k h_k = T$. We let $T = 0.8$ on CIFAR10 and $T = 0.4$ on Imagenet-32.

Network architecture: We use the softplus activation with $\beta = 20$ for all hidden layers. On MNIST, we use fully-connected residual blocks with three hidden layers at 256 hidden nodes. On CIFAR10 and Imagenet-32, we parametrize each $\mathbf{f}_{\theta_b}$ as a concatenation of convolution layers and transposed convolution layers. Specifically:

- CIFAR10: convolution layers have channels `3-64-128-256-256` with kernel size 3 and strides `1-1-2-1`. Transposed convolution layers have channels `256-256-128-64-3` with kernel size `3-4-3-3` and strides `1-2-1-1`. Total 2.1M parameters.
- Imagenet-32: convolution layers have channels `3-64-128-256-512` with kernel size 3 and strides `1-1-2-1`. Transposed convolution layers have channels `512-256-128-64-3` with kernel size `3-4-3-3` and strides `1-2-1-1`. Total 3.3M parameters.

We remark that because inputs into the JKO-iFlow blocks are latent-space codes that have much lower dimensions than the original image, our JKO-iFlow blocks are simpler and lighter in design than models in previous NeuralODE [Grathwohl et al., 2019, Finlay et al., 2020] and diffusion model works [Ho et al., 2020, Song et al., 2021, Boffi and Vanden-Eijnden, 2023]. For instance, the DDPM model [Ho et al., 2020] on CIFAR10 has 35.7M parameters with more sophisticated model designs.

Training specifics: On MNIST, we fix the batch size to be 2000 during training, and we train 15K batches per JKO-iFlow block. We fix the learning rate to be 1e-3.

On CIFAR10 and Imagenet-32, we fix the batch size to be 512 during training, and we train 75K batches per JKO-iFlow block. The time per batch is 0.18 second on Imagenet-32 and 0.15 second on CIFA10. The total time on Imagenet-32 is 30 hours and on CIFAR10 is 24 hours. When training the blocks, the initial learning rate `lr0` is decreased by a constant factor of 0.9 every 2500 batches. We let `lr0` be 1e-3 when training the first 5 blocks on Imagenet-32 and decrease it to be 8e-4 on blocks 6-8. We let `lr0` be 1e-3 when training the first 2 blocks on CIFAR10 and decrease it to be 7.5e-4 on the rest 6 blocks. Additionally, we use gradient clipping of max norm 1 after collecting gradients on each mini-batch.

Additional results: We perform the following steps to curate generated samples for CIFAR10 and Imagenet-32, which are shown in Figure 3, we first train an image classifier (i.e., VGG-16 [Simonyan and Zisserman, 2015]) on the training data. Then, we generate a large number of uncurated images (200K for Imagenet-32 and 20K for CIFAR10), classify them using the pre-trained classifier, and sort them based on top-1 predicted probability. Out of the top 20K images for Imagenet-32 and top 750 images for CIFAR10 upon sorting, we manually select images that we think most resemble the given predicted class. Figure A.7 further shows uncurated images on CIFAR10 and Imagenet-32 by the same JKO-iFlow model after training.

C.2.4 Conditional generation

To modify the JKO-iFlow to apply to the conditional generation task, we follow the framework in Xu et al. [2022], which trains a single flow mapping from X to H that pushes to match each component of the distribution associated with a distinct output label value $Y = k$, $k = 1, \cdots, K$. Specifically, for a data-label pair $\{X_i, Y_i\}$, consider the continuous ODE trajectory $x(t)$ starting from $x(0) = X_i$, the per-sample training objective is by changing the term $V(x(t_{k+1}))$ in (8) to be $V_{Y_i}(x(t_{k+1}))$, where $V_k(\cdot)$ is the potential of the Gaussian mixture component $H|Y = k$. Because the Gaussian mixture is parametrized by mean vectors (the covariance is isotropic with fixed variance) [Xu et al., 2022], the expression of $V_k(\cdot)$ is a quadratic function with explicit expression.

Training and test data:

- For the simulated two-moon data, we re-sample 5K training samples every epoch, for a total of 40 epochs per block. The batch size is 1000.

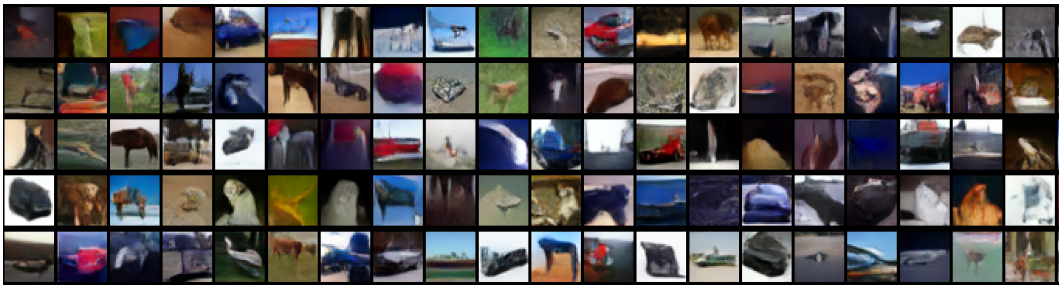

(a) Generated CIFAR10 images

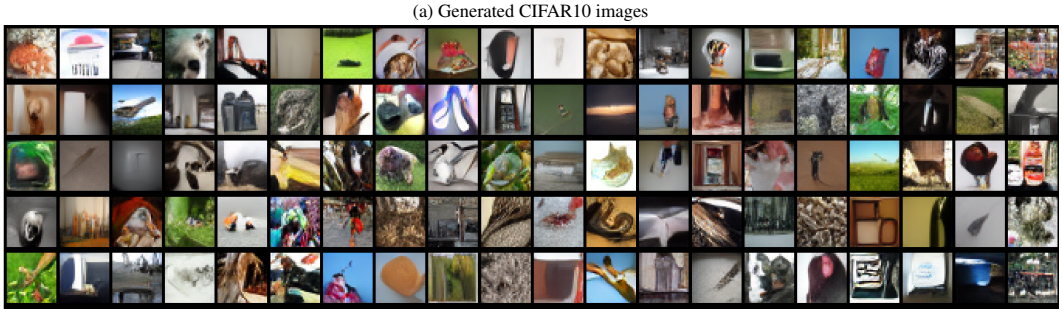

(b) Generated Imagenet-32 images

Figure A.7: Uncurated generated samples of CIFAR10 and Imagenet-32 by JKO-iFlow in latent space.

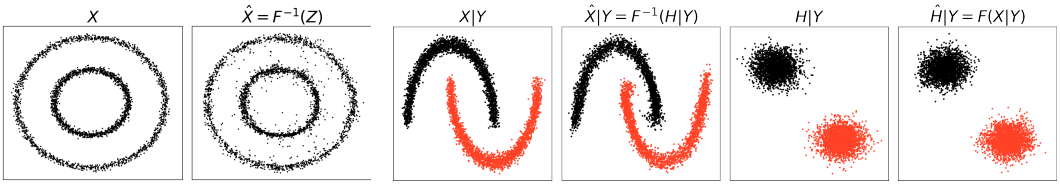

(a) Two-circles data (unconditional)

(b) Two-moons data (conditional)

Figure A.8: Unconditional and conditional generation on simulated toy datasets by JKO-iFlow. We color samples in (b) by the class label Y taking binary values. In both (a) and (b), the generated samples are close to the true samples in distribution. In (b), the pushforward distribution by JKO-iFlow, denoted as $\hat{H}|Y$, is also close to the target Gaussian mixture distribution $H|Y$.

- The solar dataset is retrieved from the National Solar Radiation Database (NSRDB), following the data pre-processsing in [Xu et al., 2022]. The dataset has 1K training sample and 1K test sample. The batch size is 500 and each block is trained 50 epochs.

Choice of h_k: For both datasets, $h_0 = 1, \rho = 1, h_{\max} = 3$. The reparametrization and refinement techniques are not used.

MMD metric: The MMD values are computed for each specific value of Y (across all graph nodes). When Y is fixed, we retrieve test samples from true data, denoted as $\boldsymbol{X}|Y$, and generate model distribution samples, denoted as $\tilde{\boldsymbol{X}}|Y$, and then compute the MMD values same as in the unconditional case. Due to the relatively small sample size of $\boldsymbol{X}|Y$ (679 and 144 respectively),

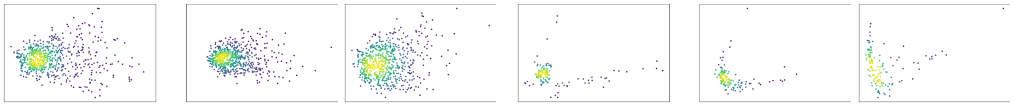

(a) True $X\|Y$	JKO-iFlow	(b) IGNN	(c) True $X\|Y$	JKO-iFlow	(d) IGNN
τ: **2.13e-3**, MMD-m:	8.12e-3	5.70e-2	τ: **2.88e-3,** MMD-m:	4.00e-2	7.67e-2
NLL	-13.60	-4.55	NLL	-4.19	1.53

Figure A.9: Conditional graph nodal data generation by JKO-iFlow and iGNN on Solar ramping data. The nodal data $X \in \mathbb{R}^{10\times 2}$ and the nodal label $Y \in \{0,1\}^{10}$. Plots (a)(b) and (c)(d) are for two different sets of values Y across all nodes respectively. Samples X (concatenated across all nodes) are visualized by projection to two principal components (determined by true samples $X|Y$).

we report the average values of MMD-m and threshold τ over 50 replicas, and in each replica, we subsample 90% observations of $\boldsymbol{X}|Y$ and generate $M = 2000$ samples to form $\tilde{\boldsymbol{X}}|Y$. For the results in Figure A.9, for the Y in plots (a)(b), $N = 612$ samples are randomly sampled from $\boldsymbol{X}|Y$ in each replica, and the standard deviation of MMD-m values is less than the 2e-3 level. For the Y in plots (c)(d), $N = 130$ samples are randomly sampled from $\boldsymbol{X}|Y$ in each replica, and the standard deviation of MMD-m values is less than the 5e-3 level. The median distance kernel bandwidth computed on the entire $\boldsymbol{X}|Y$ is used in computing the MMD values.

Network and activation: Regarding design of residual blocks,

- On two-moon data, we use fully-connected residual blocks with two hidden layers under 128 hidden nodes. The activation is Tanh. We train 4 residual blocks. Learning rate is 5e-3.
- On solar data, we follow the same design of residual blocks as [Xu et al., 2022]. More precisely, each residual block contains one Chebnet [Defferrard et al., 2016] layer with degree 3, followed by two fully-connected layers with 64 hidden nodes. The activation is ELU. We train 11 residual blocks. Learning rate is 5e-3.